

國立交通大學

光電工程研究所

博士論文

以金屬有機化學氣相沈積法成長

長波長面射型雷射

Long Wavelength Vertical Cavity Surface  
Emitting Laser Grown by Metal Organic  
Chemical Vapor Deposition



研究生: 盧廷昌

Student: Tien-chang Lu

指導教授: 王興宗

Advisor: Shing-chung Wang

中華民國九十三年六月

以金屬有機化學氣相沈積法成長  
長波長面射型雷射

**Long Wavelength Vertical Cavity Surface  
Emitting Laser Grown by Metal Organic  
Chemical Vapor Deposition**

研究生: 盧廷昌

Student: Tien-chang Lu

指導教授: 王興宗

Advisor: Shing-chung Wang



**A dissertation**

**Submitted to Institute of Electro-Optical Engineering  
College of Electrical Engineering and Computer Science  
National Chiao Tung University**

**In Partial Fulfillment of the Requirements**

**For the Degree of**

**Doctor of Philosophy**

**In Electro-Optical Engineering**

**June 2004**

**Hsin-chu, Taiwan, Republic of China**

中華民國九十三年六月

# 國立交通大學

## 論文口試委員會審定書

本校光電工程研究所博士班 盧廷昌 君

所提論文 以金屬有機化學氣相沈積法成長長波長面射型雷射

合於博士資格標準、業經本委員會評審認可。

口試委員：吳孟奇 許根玉  
吳孟奇教授 許根玉教授  
郭浩中 張振雄  
郭浩中助理教授 張振雄教授  
彭隆瀚 謝文峰  
彭隆瀚教授 謝文峰教授  
蘇炎坤  
蘇炎坤教授

指導教授：王興宗  
王興宗教授

所長：賴添元 教授

中華民國 93 年 6 月 15 日

Institute of Electro-Optical Engineering  
National Chiao Tung University  
Hsinchu, Taiwan, R.O.C.

Date : 2004/6/15

We have carefully read the dissertation entitled Long Wavelength Vertical Cavity Surface Emitting Laser Grown by Metal Organic Chemical Vapor Deposition submitted by Tien-chang Lu in partial fulfillment of the requirements of the degree of DOCTOR OF PHILOSOPHY and recommend its acceptance.

Meng-Chyi Wu

Kuo-Yuh Hsu

Hou-chung Kuo

Sheng-Tsun Huang

Lung-Han Peng

Wei-Deng Hsieh

Jian-Li Su

Thesis Advisor : S.C. Wang

Director of Institute of Electro-Optical Engineering :

Jian-Ping Shi

# 以金屬有機化學氣相沈積法成長長波長面射型雷射

研究生：盧廷昌

指導教授：王興宗 教授

國立交通大學光電工程研究所

## 摘要

本論文在研究以金屬有機化學氣相沉積法(Metalorganic chemical vapor deposition, MOCVD)製作長波長面射型雷射。波長範圍在 1.3 到 1.5 微米的面射型雷射，因其具有圓形光束輸出、低製作成本、單一縱膜操作、以及整合二維陣列的潛在特性，因此在光纖通信及中、短距數據通信上，成為極具潛力的發光源。但因在傳統製作長波長雷射的材料中，不容易找到具有折射率差異大的材料組合以製作高反射率的布拉格反射鏡，加上傳統長波長雷射的主動層材料，其高溫特性不佳，使得長波長面射型雷射的發展遲緩。

因此，在本研究中，我們從最基本的設計與模擬出發，先找出適合長波長雷射主動層的材料，然後將主動層材料應用在傳統邊射型雷射上，變化各種參數，我們發現量子井中的應力參數、多量子井的應力補償、以及參雜條件的多寡皆會影響雷射特性，我們優化各項參數，得到最好的臨界電流密度為 1.4 kA/cm<sup>2</sup>。另一方面，我們使用 MOCVD 成長磷化銦系列的布拉格反射鏡，以優化過的磊晶參數成功製作出高反射率的布拉格反射鏡，並研究其光學及電氣特性。同時，我們也嘗試製作以磷化銦搭配空氣，在只有三對組合下成功得到高反射率的布拉格反射鏡。

為了要製作出擁有良好溫度效應的長波長面射型雷射，我們也發展了晶圓融合的技術將長波長雷射主動層的材料和砷化鎵系列的布拉格反射鏡結合成長波長面射型雷射，我們成功的製作出以光激發的方式操作的融合型長波長面射型雷射，其等效的臨界電流密度為 4 kA/cm<sup>2</sup>。最佳的等效臨界電流密度值是以磷化銦系列的布拉格反射鏡，加上週期性增益之共振腔，再加上以介電材料製成的布拉格反射鏡組合而成的長波長面射型雷射，以連續光激發的方式操作，其等效的臨界電流密度為 2 kA/cm<sup>2</sup>，雷射波長為 1562 奈米。

我們最終的目的是要製作出電激發式的長波長面射型雷射，雖然在本研究中尚未達成這個目標，但為發展製作電激發式的長波長面射型雷射的過程中，我們發展了磊晶再成長技術、埋藏式穿透界面元件等技術，成功應用在長波長發光二極體，另外，我們同時也遇到了量子井相互擴散的情況、觀察到在傳統氧化侷限面射型雷射中的雙模態情形，這些研究都提供了良好的基礎朝向製作出電激發式的長波長面射型雷射。

# Long Wavelength Vertical Cavity Surface Emitting Laser Grown by Metal Organic Chemical Vapor Deposition

Student: Tien-chang Lu

Advisor: Dr. Shing-Chung Wang

Institute of Electro-Optical Engineering  
National Chiao Tung University

## Abstract

In this study, we have developed the process for fabrication of long wavelength vertical cavity surface emitting lasers (LW-VCSELs) by metal organic chemical vapor deposition (MOCVD). LW-VCSELs with emission wavelength ranging from 1.3  $\mu\text{m}$  to 1.5  $\mu\text{m}$  featuring circular-beam output, low production-cost, single longitudinal-mode operation, and possible integration of two-dimensional array are potentially suitable for light sources in fiber communication systems and in medium and short distance data transmission systems. However, the absence of high refractive index contrast in InP-lattice-matched materials impeded the development of 1.3-1.5  $\mu\text{m}$  VCSELs. In addition, active layers with insufficient gain at elevated temperature, absence of natural oxidized current aperture and poor heat conductance in material systems for long wavelength range are problems in making LW-VCSELs.

Therefore, we started this study from design and simulation to obtain appropriate gain materials for LW-VCSELs. We have determined InGaAlAs as the gain material and applied it into the conventional edge emitting lasers to find out the optimized conditions of the active layers. The amount of compressively strain in quantum wells, the net amount of strain in multiple quantum wells (MQWs) with more pairs, and the

impurity concentration strongly influenced the performance of edge emitting lasers. The overall optimization of these factors makes us obtaining low threshold current density of  $1.4 \text{ kA/cm}^2$ . On the other hand, we have fabricated InP/InGaAlAs-based distributed Bragg reflectors (DBRs) with excellent electrical and optical properties using MOCVD and the growth interruption technique. Meanwhile, we have successfully fabricated, and demonstrated a rigid InP/airgap structure with high reflectivity at  $1.54 \mu\text{m}$  using InGaAs as the sacrificial layer. The 3-pair InP/airgap DBR structure has a peak reflectivity at  $1.54 \mu\text{m}$  with a stop-band width of about 200 nm.

In addition, we have developed wafer-fusion technique to combine the conventional InP-based active layers with GaAs-based DBRs in order to simultaneously have the superior gain performance of InP-based active layers and the high reflectivity, high thermal conductivity and capability of oxidized layers of the GaAs-based DBRs. We demonstrated the optically pumped VCSEL structure with the fused bottom 30 pairs GaAs/AlAs DBR, InGaAlAs MQW and the fused top 25 pairs GaAs/AlAs DBR. The equivalent threshold current density is calculated to be  $4 \text{ kA/cm}^2$ . The lowest threshold was obtained in InP-based LW-VCSELs. We successfully demonstrated the optically pumped InP-based VCSELs with the 35 pairs InP/InGaAlAs DBRs and 10 pairs  $\text{SiO}_2/\text{TiO}_2$  top dielectric mirrors and a  $2\lambda$  thick cavity composed of periodic strain compensated MQWs to fully utilize the gain in every quantum well. The optically pumped VCSELs operated at room temperature with equivalent threshold current density calculated to be  $2 \text{ kA/cm}^2$ . The wavelength of the output beam is 1562 nm.

Although our goal to fabricate electrically driven continuous wave LW-VCSELs with single mode operation has yet to be fulfilled, this process has led to many other developments. For example, we have developed the MOCVD regrowth technique to fabricate buried tunnel junction devices and have applied this technique to fabricate long wavelength light emitting diodes with buried tunnel junction. At the same time, we have studied the quantum well inter-mixing effect, and the coexisting two-cavity configuration in conventional oxide confined VCSELs. All in all, basic physical phenomenon and material issues observed in this study will turn into useful information in making electrically driven LW-VCSELs in the future.





# CONTENTS

Abstract		i
(in Chinese)		
Abstract		ii
Acknowledgement		v
Contents		vi
List of tables		ix
List of figures		x
<b>CHAPTER 1</b>	<b>Introduction</b>	
1-1	Background	1
1-2	Development of LW-VCSELs	3
1-3	Overview of this Thesis	5
	<i>References</i>	8
<b>CHAPTER 2</b>	<b>Principal Issues in Design of Long Wavelength Vertical Cavity Surface Emitting Lasers</b>	
2-1	General Characteristics in Semiconductor Lasers	19
	Semiconductor Laser Oscillation Conditions	19
	General Characteristics of VCSELs	23
	Transverse Modes in VCSELs	25
2-2	Modeling the Gain Mediums	27
	Optical Gain in Semiconductors	27
	Optical Gain in Quantum Well Structures	30
	Nonradiative Transitions	32
	Optical Gain in Strained Quantum Wells	33
2-3	Characteristics of Distributed Bragg Reflectors	35
	Transfer Matrix Method	35
	Reflection Delay and Penetration Depth of DBRs	38
2-4	Analysis of the Heat Flow	40
2-5	LW-VCSEL Designs	42
	<i>References</i>	45
<b>CHAPTER 3</b>	<b>Fabrication of Long Wavelength Vertical Cavity Surface Emitting Lasers</b>	
3-1	Metal Organic Chemical Vapor Deposition System	73
	Reaction Equations	73
	Gas Blending Systems	74
	Reactor Chamber	75
	Uniformity Issue	76
	In-situ Monitoring	77
3-2	Epitaxial Regrowth Techniques	78
3-3	Wafer Fusion Techniques	79
	Introduction to Fusion Methods	80
	Key Issues in Wafer Fusion Process	81
	Wafer Fusion System	81
	Experiments for Fusion System Test	82

	<i>References</i>	84
<b>CHAPTER 4</b>	<b>Optimization of the Active Layers</b>	
4-1	Comparisons between Gain Materials in Long Wavelength Range	99
	GaAs-Based Gain Materials	99
	InP-Based Gain Materials	101
4-2	Characterization and Optimization of the Active Layers	102
	Fabrication of Long Wavelength FP EELs	102
	The Effect of Strain	104
	The Effect of QW number	105
	The Effect of P-type Doping Amount	107
	<i>References</i>	108
<b>CHAPTER 5</b>	<b>Fabrication of the Distributed Bragg Reflectors</b>	
5-1	Comparisons of InP/InGaAlAs and InAlAs/InGaAlAs Distributed Bragg Reflectors	121
	Introduction	121
	Experimental Procedure	123
	Results and Discussion	124
5-2	Distributed Bragg Reflectors for Long Wavelength VCSELs using InP/Air-gap	128
	Design and Fabrication	128
	Optical Characterization	131
	Thermal Analysis of LW-VCSELs with Air-gap Reflectors	131
	<i>References</i>	135
<b>CHAPTER 6</b>	<b>Optically Pumped LW-VCSELs</b>	
6-1	Structures and Characteristics of Optically Pumped LW-VCSELs Based on InP/InGaAlAs DBRs	153
	The Structure of LW-VCSEL	153
	The Results of Optical Pumping	154
6-2	Structures and Characteristics of Optically Pumped LW-VCSELs with Wafer-fused GaAs/AlAs DBRs	155
	Influence of Distance between Fusion Interface and Active Region	156
	Comparisons of Spectra before and after Wafer Fusion Process	157
	Optical Pumping of VCSEL Structure with Double-fused DBRs	158
	<i>References</i>	160
<b>CHAPTER 7</b>	<b>Electrically Driven LW-VCSELs</b>	
7-1	Fabrication of LW-VCSELs by Ion-implantations	173
	The Structure of LW-VCSEL	173
	Results and Discussion	174
7-2	Long Wavelength Light Emitting Diodes with Buried	

	Tunnel Junctions	175
	Introduction	175
	The Structure of Long Wavelength LEDs with Buried Tunnel Junctions	176
	Results and Discussion	177
7-2	Fabrication of LW-VCSELs by Wafer Fusion Techniques	177
	Quantum Well Inter-mixing	177
	The Structure of LW-VCSELs by Wafer Fusion Techniques	178
	Results and Discussion	179
	<i>References</i>	180
<b>CHAPTER 8</b>	<b>Conclusions and Future Works</b>	
	Conclusions	191
	Future Works	193
<b>APPENDIXES</b>		
A-1	Introduction to Laser Simulation Software	197
	<i>References</i>	199



## List of tables

<b>Table 1-1</b>	Comparison of features for EEL vs VCSEL	11
<b>Table 2-1</b>	Comparison of threshold conditions for EEL vs VCSEL.	47
<b>Table 2-2</b>	Magnitude of $ \mathbf{M} ^2$ for various material systems.	48
<b>Table 2-3</b>	Magnitude of $ \mathbf{M}_T ^2/ \mathbf{M} ^2$ for different transitions and polarizations.	49
<b>Table 2-4</b>	Various material combinations for making high reflectivity DBRs	50



## List of figures

### Chapter 1

<b>Figure 1-1</b>	Spectral loss profile of a typical single-mode silica fiber.	13
<b>Figure 1-2</b>	Typical wavelength dependence of the dispersion parameter.	14
<b>Figure 1-3</b>	Progress in lightwave communication technology over the period 1974-1996.	15
<b>Figure 1-4</b>	Bandgap versus lattice constant for III-V compound semiconductors used in LW-VCSELs.	16
<b>Figure 1-5</b>	Three LW-VCSEL structures:	17

### Chapter 2

<b>Figure 2-1</b>	Schematics of edge emitting lasers.	51
<b>Figure 2-2</b>	Typical semiconductor laser output power vs. injection current relation (L-I curve).	52
<b>Figure 2-3</b>	The gain, optical mode and power spectrum for a Fabry-Perot laser.	53
<b>Figure 2-4</b>	Operation of a Fabry-Perot laser.	54
<b>Figure 2-5</b>	General schematics of VCSELs.	55
<b>Figure 2-6</b>	The gain and optical mode spectrum for a VCSEL.	56
<b>Figure 2-7</b>	Schematics of alignment between gain and cavity mode peak at different temperature.	57
<b>Figure 2-8</b>	Schematics of optical waveguide for oxide VCSEL.	58
<b>Figure 2-9</b>	The spectrum and near field spontaneous emission patterns of the oxide-confined VCSEL with a $6 \times 6 \mu\text{m}$ square aperture operated at $0.9 I_{\text{th}}$ ( $\sim 1 \text{ mA}$ ).	59
<b>Figure 2-10</b>	The relationship between energy and k-space and illustration of k-selected transition in parabolic shape band structure.	60
<b>Figure 2-11</b>	Illustration of an incident light gaining its power after passing through a portion of gain medium	61
<b>Figure 2-12</b>	Allowed and forbidden transitions in a quantum well.	62
<b>Figure 2-13</b>	Valence band structures of unstrained bulk semiconductor such as GaAs	63

<b>Figure 2-14</b>	Three major types of nonradiative recombination paths	64
<b>Figure 2-15</b>	Illustration of thin epilayer of lattice constant $a_c$ grown under biaxial compression and tension on substrate with lattice constant $a_s$ .	65
<b>Figure 2-16</b>	Qualitative band energy shift of the conduction band and three valence bands for biaxial compressive and tensile strain.	66
<b>Figure 2-17</b>	Band-edge profiles in real space with different strain.	67
<b>Figure 2-18</b>	Schematics of plane wave incident on thin films on a substrate.	68
<b>Figure 2-19</b>	The simulated results for a stack of InGaAlAs/InAlAs DBRs with 10, 20, 30, and 40 pairs.	69
<b>Figure 2-20</b>	The illustration of the penetration depth concept.	70
<b>Figure 2-21</b>	The simulated electric field in 40 pairs InGaAlAs/InAlAs DBRs.	71
<b>Figure 2-22</b>	The main categories of considerations in designing the LW-VCSELs.	72

### Chapter 3

<b>Figure 3-1</b>	Major components of a low pressure MOCVD system.	87
<b>Figure 3-2</b>	Components of a low pressure MOCVD system	88
<b>Figure 3-3</b>	Schematics of gas blending system in MOCVD.	89
<b>Figure 3-4</b>	Schematics of reactor design in MOCVD system.	90
<b>Figure 3-5</b>	The reflectivity mapping of the AlAs/GaAs DBRs grown with various alkyl inject mass flow controller settings.	91
<b>Figure 3-6</b>	Schematic of in-situ monitoring configuration and the measured reflectivity of calibration layers and DBR layers.	92
<b>Figure 3-7</b>	Procedure for fabrication of buried heterojunction laser diodes.	93
<b>Figure 3-8</b>	The bird's view of the surface after the regrowth process and the cross-section of the buried ridge taken by the SEM.	94
<b>Figure 3-9</b>	The schematic drawing of the fusion fixture.	95
<b>Figure 3-10</b>	The apparatus of wafer fusion system.	96
<b>Figure 3-11</b>	Optical microscope picture and SEM image of GaAs/InP	97

interface.

## Chapter 4

<b>Figure 4-1</b>	The simulated gain-wavelength and gain-carrier relationships for InGaAlAs and InGaAsP strained compensating quantum wells.	109
<b>Figure 4-2</b>	The simulated band diagrams under forward bias for InGaAlAs and InGaAsP multiple quantum wells.	110
<b>Figure 4-3</b>	The epitaxial structure for 1550 nm FP lasers and the schematic of band diagram.	111
<b>Figure 4-4</b>	The schematics of process flow for simple ridge FP lasers.	112
<b>Figure 4-5</b>	The SEM cross-sectional image of the 1550 nm laser ridge.	113
<b>Figure 4-6</b>	The temperature dependence of the threshold current for both 1310 nm and 1550 nm FP lasers.	114
<b>Figure 4-7</b>	The dependence of the laser threshold current density on the amount of compressive strain in quantum wells.	115
<b>Figure 4-8</b>	The X-ray diffraction patterns of different strain-compensated MQWs.	116
<b>Figure 4-9</b>	The simulated valence band structure for 2.0% strain and 0.7% strain in quantum wells.	117
<b>Figure 4-10</b>	The effect of quantum well numbers on the laser threshold current and confinement factor.	118
<b>Figure 4-11</b>	The effect of the flow rate of p-type dopant on the laser threshold current.	119

## Chapter 5

<b>Figure 5-1</b>	The pit density of 10 pairs InP/InGaAlAs DBRs grown with different interruption time $t_p$ , and the cross section the InP/InGaAlAs DBRs grown with 0.1-minute interruption time investigated by SEM.	137
<b>Figure 5-2</b>	The reflectivity curves of 10 pairs InP/InGaAlAs DBRs grown with different interruption time $t_p$ .	138
<b>Figure 5-3</b>	The X-ray diffraction patterns of 10 pairs InP/InGaAlAs DBRs grown with different interruption time $t_p$ .	139
<b>Figure 5-4</b>	The SIMS results of InP/InGaAlAs DBRs grown with $t_p$	140

= 0.2 minute.

<b>Figure 5-5</b>	The interface conditions of InP/InGaAlAs DBRs examined by TEM with different growth interruption time.	141
<b>Figure 5-6</b>	The I-V curves of InP/InGaAlAs DBRs and InAlAs/InGaAlAs DBRs and the simulation of the equilibrium band diagrams.	142
<b>Figure 5-7</b>	The reflectivity curves of 35 pairs InP/InGaAlAs and InAlAs/InGaAlAs DBRs measured by spectrometer.	143
<b>Figure 5-8</b>	The reflectivity of three-pair of InP/airgap DBR structure with a fixed $\lambda/4$ InGaAs layer and different InP layer.	144
<b>Figure 5-9</b>	Schematic diagram of the fabrication procedure of the InP/airgap DBRs.	145
<b>Figure 5-10</b>	The cross section of the stable suspended InP/airgap DBRs captured by SEM.	146
<b>Figure 5-11</b>	The calculated and measured reflectivity curves of the InP/airgap DBRs.	147
<b>Figure 5-12</b>	The schematic cross section of LW-VCSEL with air-gap and dielectric reflectors.	148
<b>Figure 5-13</b>	The temperature distribution and the heat flow pattern simulated by FEA tool based on the heat-transferred modal.	149
<b>Figure 5-14</b>	The influences of the radius of undercut, thickness of InP spacer, thickness of n-InP spacer, and thickness of metal contact, on the values of the thermal resistance.	150
<b>Figure 5-15</b>	The threshold gain versus the thickness of the n-InP and p-InP spacer layers.	151

## Chapter 6

<b>Figure 6-1</b>	Schematic cross section of VCSELs.	161
<b>Figure 6-2</b>	Reflectance and PL spectrum VCSEL structure.	162
<b>Figure 6-3</b>	Schematic setup of optical pumping.	163
<b>Figure 6-4</b>	The VCSEL output power versus input laser pumping power characteristics at room temperature and the VCSEL emission spectrum at the pumping power above the threshold.	164
<b>Figure 6-5</b>	Process for fused-MQW for quality experiment.	165
<b>Figure 6-6</b>	Dependence of the PL peak intensity on the distance	166



from the fusion interface.

<b>Figure 6-7</b>	Flowchart of MQW/DBR fusion process.	167
<b>Figure 6-8</b>	PL spectra of MQW before and after wafer fusion.	168
<b>Figure 6-9</b>	The DBR reflectivity spectra before and after fusion.	169
<b>Figure 6-10</b>	Process flow chart of double fused VCSEL.	170
<b>Figure 6-11</b>	The refractive index distribution of the wafer-fused VCSELs and the simulation of the electric field inside the VCSEL structure.	171
<b>Figure 6-12</b>	The double fused VCSEL output power versus input pumping laser power density characteristics at room temperature.	172

## Chapter 7

<b>Figure 7-1</b>	Schematics of LW-VCSEL with Si-implanted current aperture.	181
<b>Figure 7-2</b>	The voltage and emission light output versus driving current characteristics for InP-based LW-VCSELs with Si-implantation.	182
<b>Figure 7-3</b>	The reflectivity and PL curves of the LW-VCSEL with Si-implantation.	183
<b>Figure 7-4</b>	Detailed descriptions of epitaxial structure for long wavelength LED with tunnel junction.	184
<b>Figure 7-5</b>	Schematics of long wavelength LED structure with buried tunnel junction and the top view of the long wavelength LED before and after electrical operations.	185
<b>Figure 7-6</b>	The voltage and emission light output versus driving current characteristics for the long wavelength LED with buried tunnel junction.	186
<b>Figure 7-7</b>	Effect of quantum well inter-mixing.	187
<b>Figure 7-8</b>	Schematics of double fused LW-VCSEL with proton-implanted current aperture.	188
<b>Figure 7-9</b>	The top emission image and the EL spectrum measured from the top surface of the LW-VCSEL with proton-implanted current aperture.	189

# CHAPTER 1

## Introduction

### 1-1 Background

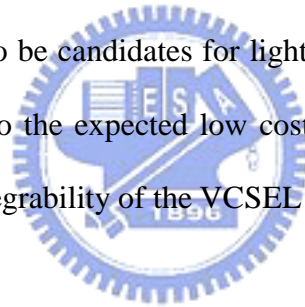
In nowadays, the worldwide interconnections via the digital information streams have deeply influenced people's life in many aspects, such as the rapid economic development, the knowledge share and flow, the way of learning and even the way of thinking. The basic infrastructures for the modern worldwide interconnections rely on the optical communication systems. Dated back to the 70's, two breakthroughs had made great advances in optical communication systems. One is the successful continuous-wave (CW) operation of the semiconductor laser at the room temperature [1]. The semiconductor lasers can be directly modulated with information and provide compact and reliable light sources for optical communication systems. The other breakthrough is the improved fabrication technique of the optical fibers leading to the reduced transmission loss from 150 dB/km to 20 dB/km. The subsequent investigation in optical fibers shows a low transmission loss window in the wavelength range near the infrared band. Figure 1-1 shows that intrinsic material absorption for silica fiber is less than 0.03 dB/km in the 1.3- to 1.6- $\mu\text{m}$  wavelength window. In addition to the fiber loss, chromatic dispersion limits the performance of lightwave systems. For standard single mode fiber, the typical wavelength dependence of the dispersion parameter is shown in Figure 1-2. The zero dispersion wavelength locates at 1.3  $\mu\text{m}$ . To further utilize the lowest loss band of fibers in 1.55  $\mu\text{m}$ , dispersion flattened and dispersion shifted fibers with specialized structures have been introduced. Figure 1-3 shows that these advances accompanied with developments of semiconductor lasers and detectors demonstrate superior

performance in the long wavelength range from 1.3 to 1.6  $\mu\text{m}$  than in the short wavelength at around 0.8  $\mu\text{m}$ .

Since the first successful CW double-heterojunction (DH) semiconductor laser had been demonstrated, commercial applications of edge-emitting lasers (EEL) have become practical. For this type of design, the optical gain was provided by electron-hole recombination in the active region, and cleaved facets perpendicular to the junction plane provided the optical feedback. The subsequent progress, such as improvement of epitaxial techniques, better material quality, utilization of the quantum wells (QW) active region, and the invention of distributed feedback (DFB) lasers, fulfill the stringent requirements in optical communication systems.

In the late 70s, Iga *et al.* [3] had proposed a semiconductor laser oscillating perpendicular to the device surface plane, which is termed vertical cavity surface emitting laser (VCSEL) in contrast to EELs. VCSELs have demonstrated many advantages over EELs. First, the monolithic fabrication process and wafer-scale probe testing as per the silicon semiconductor industry substantially reduces the manufacturing cost because only known good devices are kept for further packaging [4]. Second, a densely packed two-dimensional laser array can be fabricated because the device occupies no larger of an area than a commonly used electronic device [5]. Third, the microcavity length allows inherently single longitudinal cavity mode operation due to its large mode spacing. Temperature-insensitive devices can therefore be fabricated with an offset between the wavelength of the cavity mode and the active gain peak [6]. Finally, the device can be designed with a low numerical aperture and a circular output beam to match the optical mode of an optical fiber, thereby permitting efficient coupling without additional optics [7]. Some additional advantages of VCSELs with respect to EELs are listed in Table 1-1.

As the nearly completion of long haul interconnection in optical communication system around the world, how to further increase the bit rate and how to access through “the last mile” become demanding. The optical amplification for increasing the repeater spacing and the wavelength-division multiplexing (WDM) can further boost the bit rate. In the metropolitan connections or local area network (LAN) applications for gigabit ethernet and fiber to the home (FTTH), a high speed, low threshold, low cost long wavelength vertical cavity surface emitting lasers (LW-VCSEL) is much anticipated. Because of the larger distance-bandwidth product achievable in silica-based fiber at 1.3  $\mu\text{m}$ , the maximum data-transmission rate and point-to-point distance in these links is expected to increase more than two times with the introduction of multimode 1.3  $\mu\text{m}$  VCSELs. Single-mode VCSELs operating at both 1.3 and 1.55  $\mu\text{m}$  can also be candidates for light sources in telecommunications and WDM applications due to the expected low cost of VCSELs, the possibility of fabricating arrays, and the integrability of the VCSEL structure.



## **1-2 Development of LW-VCSELs**

GaAs-based VCSELs operating in the short wavelength range (0.78-0.98  $\mu\text{m}$ ) have exhibited tremendous progress in their performance over the past few years. Although the first VCSEL operated at 1.3  $\mu\text{m}$  [3], the development of long wavelength VCSELs (operated at 1.3-1.5  $\mu\text{m}$ ) have been slower over the past years in comparison to GaAs-based VCSELs owing to several difficulties. The key issues have been the difficult realization of high reflectivity mirrors in the long wavelength range and of active layers with sufficient gain at elevated temperature. The corresponding problems are absence of natural oxidized current aperture and poor heat conductance in material systems for long wavelength range. As shown in Figure 1-4, appropriate

material systems used for long wavelength range lattice-match to InP. Unfortunately, the InGaAsP material systems lattice-matched to InP for gain medium have pronounced low characteristic temperature due to serious auger recombination and inter-valence band absorption in active region. The problem with the conventional InP-lattice-matched InP/InGaAsP and InAlAs/InGaAlAs is the small refractive index contrast ( $\Delta n = 0.27$  for InP/InGaAsP and  $\Delta n = 0.3$  for InAlAs/InGaAlAs) resulting in a larger number of distributed Bragg reflector (DBR) pairs required to obtain high reflectivity. In addition, using the conventional DBRs, not only the penetration depth will increase causing more absorption, but the heat dissipation is also a problem. Therefore, efforts like developing active layers with high gain, fabricating DBRs with higher reflectivity, and designing device structures with higher thermal conductance have been studied for the past years. The device structures investigated for LW-VCSELs can be divided into three groups [9]. The simplified schematics of these device structures are shown in Figure 1-5:

- (1) Etched-well VCSEL structure that use amorphous-dielectric mirrors on both-sides of active layer [10] as shown in Figure 1-5(a),
- (2) VCSEL structures with one semiconductor and one amorphous-dielectric mirror that utilize ring contacts [11] as shown in Figure 1-5(b).
- (3) All-epitaxial devices that mimic the single-grown GaAs-based VCSEL structure [12] as shown in Figure 1-5(c).

Recently, long wavelength VCSELs have been successfully demonstrated with several different approaches in all three device structures. First, wafer fusion technique, that integrated the InP-based active layers and GaAs-based DBRs together, had been successfully realized for high performance long wavelength VCSELs [13, 14]. Second, the InGaNAAs 1.3  $\mu\text{m}$  VCSELs grown on GaAs substrates have been demonstrated with excellent characteristics [15, 16], but to extend the InGaNAAs gain

peak to beyond 1.5  $\mu\text{m}$  is rather difficult. Monolithically grown DBRs lattice-matched to InP continued to attract interests due to the well existing highly efficient InGaAsP and InGaAlAs gain materials covered the wavelength window from 1.3 to 1.8  $\mu\text{m}$ . Metamorphic GaAs/AlAs DBRs lattice-matched to InP substrate have been applied to realize the long wavelength VCSELs [17, 18] but the inherent dislocations in metamorphic layers have impacts on the reliability of the devices. The Sb-based DBRs have large refractive index contrasts  $\Delta n$  ranging from 0.43 to 0.44 and have been successfully applied in the VCSEL structures [19, 20]. However, these DBRs have drawbacks such as the low thermal conductivity and relatively high growth complexity.

### **1-3 Overview of this Thesis**

This study has focused on the design of active layers, the growth of the DBRs, the process of the LW-VCSEL structures. Two different material systems have been studied. The monolithically InP-based VCSELs are chosen since the potential of single epitaxial growth ensures the practical devices for mass production. Although the capability of mass production for wafer fused VCSELs is still questionable, the excellent thermal and optical properties of GaAs/AlAs DBRs as well as the capability of the oxidation process make the wafer fused VCSELs worth of studying.

Chapter 2 reviews fundamentals in semiconductor lasers at beginning. The origin of differences between EELs and VCSELs will be discussed. Then, general operation principles of VCSELs including light-current characteristics, the relationship between gain and current, the gain peak and cavity mode alignment, the characteristics of DBRs, the analysis of the heat flow will be introduced and characterized with the use of simulation software. With specific conditions in

requirement of LW-VCSELs, the fundamental issues in design of LW-VCSELs will be discussed at the end of the chapter.

Chapter 3 mainly describes the fabrication method for LW-VCSELs. Metal organic chemical vapor deposition (MOCVD) systems have been used for growing all the epitaxial structures in this study. Since the epitaxial equipment and process determine most of the characteristics of LW-VCSELs, detailed descriptions and specific functions of this MOCVD system are given. The growth process, regrowth process and in-situ monitoring will also be addressed. Wafer fusion technique, which is the other special and important process step in fabrication of LW-VCSELs, will also be introduced.

The characteristics of gain medium suitable for LW-VCSEL have been discussed at the beginning of chapter 4. By considering material quality and limitations of process equipment, the InGaAlAs system lattice-matched to InP has been chosen as the active layers in this study. The optimized layer structures have been determined by investigating performance of EELs with InGaAlAs multiple quantum wells (MQW) as the active layers.

Chapter 5 reports several different fabrication methods for DBRs used in long wavelength range. The optical and electrical properties of different DBRs will also be studied. Followed by the comparisons of novel InP/InGaAlAs and conventional InAlAs/InGaAlAs DBRs, the extremely high reflectivity mirror made by InP/Air-gap DBRs will be discussed.

The feasibility of the active layers and DBRs is first examined by the performance of optically pumped LW-VCSELs. Chapter 6 reports the structures of LW-VCSELs for optical pumping, including the InP-lattice-matched and wafer-fused structures.

Chapter 7 reports several different approaches to make electrically driven

LW-VCSELs, including monolithically InP-based and wafer-fusion type devices. The ion-implantation or buried tunnel junction were used to make current apertures in devices. Although the goal to make electrically driven devices has not yet accomplished, efforts resulted from this study have led to develop other interesting devices. In addition, basic physical phenomenon and material issues observed in this study will turn into useful information in making electrically driven LW-VCSELs. Chapter 8 is the summary of this thesis.





## References

- [1] I Hayashi, M. B. Panish, P. W. Foy, and S. Sumuski, *Appl. Phys. Lett.*, v17, p10, 1970.
- [2] G. P. Agrawal, *Fiber-optic communication systems*. 2nd ed. John Wiley & Sons, Inc., N. Y., 1997.
- [3] H. Soda, K. Iga, C. Kitahara, and Y. Suematsu, *Jpn. J. Appl. Phys.*, v18, p2329, 1979
- [4] K. Iga, F. Koyama, and S. Kinoshita, *IEEE J. Quantum Electron.*, QE-24, p1845, 1988.
- [5] M. Orenstein, A. C. Von Lehmen, C. Chang-Hasnain, N. G. Stoffel, J. P. Harbison, and L. T. Florez, *Electron. Lett.*, v27, p437, 1991
- [6] D. B. Young, J. W. Scott., F. H. Peters, B. J. Thibeault, S. W. Corzine, M. G. Peters, S. L. Lee, and L. A. Coldren, *IEEE Photon. Tech. Lett.*, v5, p129, 1993
- [7] K. Tai, G. Hasnain, J. D. Wynn, R. J. Fischer, Y. H. Wang, B. Weir, J. Gamelin, and A. Y. Cho, *Electron. Lett.*, v26, p1628, 1990
- [8] C. DeCusatis, *Handbook of Fiber Optic Data Communication*, 2nd ed. Academic Press, 2002.
- [9] C. W. Wilmsen, H. Temkin, and L. A. Coldren, "Long-wavelength vertical-cavity lasers," in *Vertical-Cavity Surface-Emitting Lasers: Design, Fabrication, Characterization, and Applications*, Cambridge University Press, 1999.
- [10] K. Iga and F. Koyama, "Vertical-cavity surface-emitting lasers and arrays," in *Surface-Emitting Semiconductor Lasers and Arrays*, G. A. Evans and J. M. Hammer, eds., Academic Press, San Diego, 1993.
- [11] T. Tadokoro, T., H. Okamoto, Y. Kohama, T. Kawakami, and T. Kurokawa, *IEEE Photon. Technol. Lett.*, v4, no.5, p409, 1992.
- [12] D. I. Babic, K. Streubel, R. P. Mirin, N. M. Margalit, J. E. Bowers, E. L. Hu, D. E. Mars, L. Yang, and K. Carey, *IEEE Photon. Technol. Lett.*, v7, no.11, p1025, 1995.
- [13] D. I. Babic, J. Piprek, K. Streubel, R. P. Mirin, N. M. Margalit, D. E. Mars, J. E. Bowers and E. L. Hu, *IEEE J. Quantum Electron.*, v33, no.8, p1369, 1997
- [14] Y. Ohiso, C. Amano, Y. Itoh, H. Takenouchi and T. Kurokawa, *IEEE J. Quantum Electron.*, v34, no.10, p1904, 1998)
- [15] S. Sato, N. Nishiyama, T. Miyamoto, T. Takahashi, N. Jikutani, M. Arai, A

- Matsutani, F. Koyama and K. Iga, *Electron. Lett.*, v36, no.24, p2018, 2000)
- [16] G. Steinle, F. Mederer, M. Kicherer, R. Michalzik, G. Kristen, A. Y. Egorov, H. Riechert, H. D. Wolf and K.J. Ebeling, *Electron. Lett.*, v37, no.10, p632, 2001)
- [17] J. Boucart, C. Starck, F. Gaborit, A. Plais, N. Bouche, E. Derouin, J. C. Remy, J. Bonnet-Gamard, L. Goldstein, C. Fortin, D. Carpentier, P. Salet, F. Brillouet and J. Jacquet, *IEEE J. Sel. Topics Quantum Electron.*, v5, no.3, p520, 1999
- [18] W. Yuen, G.S. Li, R.F. Nabiev, J. Boucart, P. Kner, R.J. Stone, D. Zhang, M. Beaudoin, T. Zheng, C. He, K. Yu, M. Jansen, D.P. Worland and C.J. Chang-Hasnain, *Electron. Lett.*, v36, no.13, p1121, 2000
- [19] E. Hall, H. Kroemer and L.A. Coldren, *Electron. Lett.*, v35, no.5, p425, 1999
- [20] E. Hall, S. Nakagawa, G. Almuneau, J.K. Kim and L.A. Coldren, *Electron. Lett.*, v36, no.17, p1465, 2000



**Table 1-1** Comparison of features for EEL vs VCSEL [8]

<i>Feature</i>	<i>EEL</i>	<i>VCSEL</i>
Spectral bandwidth	Very narrow	Narrow
Size of active area	Typically 0.5-1×2-10 μm	Variable, 5-50 μm in diameter
Beam geometry	Strong elliptic	Circular
Beam divergence	High, up to 60°×20°	Low, 5°
Number of modes	Typically 1 or few	1 or even up to many 10s
Coupling to fiber	Difficult and sensitive	Easy
Coupling efficiency	Moderate	High
Threshold current	Approximately 10 mA	Some mA
Direct modulation bandwidth	High, up to 10 Gbit/s	High, up to 10 Gbit/s
Temperature drift of P <sub>op</sub>	Fairly high	Tendentially low
Environmental sensitivity	Extremely high	Moderate
Processing of chip	Very specific	Similar to LED
Final processing	Single bar	On wafer
Burn-in and functional test	Single on heatsink	On wafer

## CHAPTER 2

# Principal Issues in Design of Long Wavelength Vertical Cavity Surface Emitting Lasers

This chapter reviews fundamentals in semiconductor lasers at beginning. The origin of differences between edge emitting lasers (EELs) and vertical cavity surface emitting lasers (VCSELs) will be discussed. Then, general operation principals of VCSELs including light-current characteristics, the relationship between gain and current, the gain peak and cavity mode alignment, the characteristics of distributed Bragg reflectors (DBRs), the analysis of the heat flow will be introduced and characterized with the use of simulation software. With specific conditions in requirement of long wavelength vertical cavity surface emitting lasers (LW-VCSELs), the fundamental issues in design of LW-VCSELs will be discussed at the end of the chapter.



### 2-1 General Characteristics in Semiconductor Lasers

#### Semiconductor Laser Oscillation Conditions

The typical EELs shown in Figure 2-1(a) are Fabry-Perot (FP) lasers with double-heterojunction (DH) structures. The EELs, with small enough cross-section, may be initially modeled by considering a resonator, which contains plane optical waves travelling back and forth along the length of the lasers. The natural cleaved facets provide optical feedback for the laser cavity associated with the refractive index of the active layers. If the refractive index of the active layer is  $n_r$ , for the normal incident light, the reflectivity of the cleaved facet is

$$r^2 = R = \left( \frac{n_r - 1}{n_r + 1} \right)^2 \quad (2-1)$$

Assumed an electromagnetic wave travelling back and forth in the laser cavity as shown in Figure 2-1(c), the amplitude decays or grows with distance because the wave suffers scattering and other fixed losses  $\alpha_i$  per unit length, but also experiences a material optical gain  $\gamma$  per unit length provided by the electrons and holes recombining at a rate which increases with the injected carrier density. The laser cavity length is  $L$  and the wave field at point (1) can be expressed as:

$$I_1 = I_o e^{jkz_o} \quad (2-2)$$

After the wave travels through point (2), (3), (4) and backs to point (1), the wave field can be expressed as:

$$I_4 = R_1 R_2 I_o e^{2(\gamma - \alpha_i)L} e^{jk(z_o + 2L)} \quad (2-3)$$

The equilibrium wave field after one round trip must achieve for the occurrence of laser oscillation. Two oscillation conditions are obtained when  $I_1$  equals to  $I_4$ . One is the amplitude condition:

$$R_1 R_2 I_o e^{2(\gamma - \alpha_i)L} = I_o \quad (2-4)$$

The other one is phase condition:

$$e^{jk(z_o + 2L)} = e^{jkz_o} \quad (2-5)$$

$$k \cdot 2L = q \cdot 2\pi \quad (2-6)$$

where  $q$  is an integer.

From the amplitude condition (2-4), the threshold condition can be obtained:

$$\gamma_{th} = \alpha_i + \frac{1}{2L} \ln \frac{1}{R_1 R_2} \quad (2-7)$$

which explains that the threshold gain is the summation of the internal loss and the mirror loss. However, the optical wave travelling in the laser cavity does not pass all the gain region, the confinement factor,  $\Gamma$ , has to be added to modify the threshold condition:

$$\Gamma\gamma_{th} = \alpha_i + \frac{1}{2L} \ln \frac{1}{R_1 R_2} = \alpha_i + \alpha_m \quad (2-8)$$

If a linear gain approximation is assumed, the relationship between gain and carrier density can be expressed as:

$$\gamma_{th} \equiv a(n_{th} - n_{tr}) \quad (2-9)$$

where  $a$  is the differential gain,  $n_{tr}$  is the transparent current density. Assumed that thickness of the active layer is  $d$ , the threshold condition becomes:

$$\begin{aligned} \gamma_{th} &= \frac{1}{\Gamma} \left( \alpha_i + \frac{1}{2L} \ln \frac{1}{R_1 R_2} \right) = a \left( \frac{J_{th} \tau_n}{ed} - \frac{J_{tr} \tau_n}{ed} \right) \\ J_{th} &= \frac{d}{b\Gamma} \left( \alpha_i + \frac{1}{2L} \ln \frac{1}{R_1 R_2} \right) + dJ_o \\ b &\equiv \frac{a\tau_n}{e}, \quad J_o \equiv \frac{J_{tr}}{d} \end{aligned} \quad (2-10)$$

where  $\tau_n$  is the carrier lifetime,  $J_{tr}$  is the transparent current density. If the internal quantum efficiency is smaller than 1, the equation (2-10) should be modified as:

$$J_{th} = \frac{d}{\eta_i b \Gamma} \left( \alpha_i + \frac{1}{2L} \ln \frac{1}{R_1 R_2} \right) + \frac{dJ_o}{\eta_i} \quad (2-11)$$

To further explain the characteristics of laser output, the analytical rate equations have been used. Assumed the photon density in the laser cavity is  $n_{ph}$ , and the effective refractive index of the waveguide is  $n_r$ , the rate equations for carrier density,  $n$ , and the photon density,  $n_{ph}$ , can be expressed as:

$$\frac{dn}{dt} = \frac{\eta_i J}{ed} - \frac{n}{\tau_n} - g \cdot n_{ph} \quad (2-12)$$

$$\frac{dn_{ph}}{dt} = \Gamma \cdot g \cdot n_{ph} - \frac{n_{ph}}{\tau_p} + \Gamma \cdot \beta \cdot \frac{n}{\tau_n} \quad (2-13)$$

and

$$g \equiv \gamma \cdot \left( \frac{c}{n_r} \right) = a \cdot \left( \frac{c}{n_r} \right) \cdot (n - n_{tr}) \quad (2-14)$$

where  $c$  is the speed of light,  $\tau_p$  is the photon lifetime, and  $\beta$  is the spontaneous emission factor. Spontaneous emission factor represents the ratio that spontaneous

emission modes contribute to the stimulated emission modes. The value of  $\beta$  is very small that the last term of the equation (2-13) can be neglect. At the steady state, from equation (2-13),

$$\tau_p = \left(\frac{1}{g}\right) = \frac{n_r}{c} \cdot \frac{1}{\alpha_i + \frac{1}{2L} \ln\left(\frac{1}{R_1 R_2}\right)} \quad (2-15)$$

When the operation condition approaches threshold, the photon density still can be seen as zero, the equation (2-13) becomes:

$$\frac{J_{th}}{ed} = \frac{n_{th}}{\tau_n} \quad (2-16)$$

which is identical to equation (2-11). When the operation condition is above the threshold, the carrier density pins at  $n_{th}$ , and the equation (2-13) becomes:

$$\frac{n_{ph}}{\tau_p} = \frac{J - J_{th}}{ed} \quad (2-17)$$

If the laser active volume is  $V$ , which is the product of the cross-section area  $A$  and thickness of active layer  $d$ . Let equation (2-17) time  $V$  at both sides of equation. Then, the power generated by stimulated emission inside the laser cavity can be expressed as:

$$P_s = \left(\frac{n_{ph} \cdot V}{\tau_p}\right) \cdot h\nu = \eta_i \cdot \frac{h\nu}{e} \cdot (I - I_{th}) \quad (2-18)$$

Since the laser power out of the laser cavity is termed as the mirror loss, the output power can be expressed as:

$$P_o = \eta_i \cdot \frac{h\nu}{e} \cdot (I - I_{th}) \cdot \left(\frac{\frac{1}{2L} \ln\left(\frac{1}{R_1 R_2}\right)}{\alpha_i + \frac{1}{2L} \ln\left(\frac{1}{R_1 R_2}\right)}\right) \quad (2-19)$$

As shown in Figure (2-2), the slope efficiency defined as the ratio between output power over injected current is expressed as:

$$\eta_s = P_o / (I - I_{th}) = \left(\frac{h\nu}{e}\right) \cdot \eta_d \quad (2-20)$$

where  $\eta_d$  is the differential quantum efficiency, which is the ratio between number of

the increased photons over number of the injected electrons.

From the phase condition (2-4), the threshold condition can be obtained:

$$k \cdot 2L = q \cdot 2\pi$$

$$L = q \cdot \left( \frac{\lambda_o}{2n_r} \right) \quad (2-21)$$

Equation (2-21) shows that the laser oscillation wavelength is determined by cavity length. For a typical EEL, the line width of the gain spectrum is larger than the mode spacing as shown in Figure 2-3. The allowed laser modes, or longitudinal modes can be several. The mode spacing between longitudinal modes derived from equation (2-21) can be expressed as:

$$\Delta\lambda = \frac{\lambda^2}{2n_r L \left( 1 - \frac{\lambda}{n_r} \left( \frac{\partial n_r}{\partial \lambda} \right) \right)} \quad (2-22)$$

Figure 2-4 shows schematic of standing waves inside the laser cavity. Also shown in Figure 2-4 also shows that the laser output beam exhibits an elliptic shape due to the waveguide structure inside the laser cavity. The waveguide structure defines not only the optical confinement but also the carrier confinement. The optical confinement factor can be taken apart into three directions:

$$\Gamma = \Gamma_x \cdot \Gamma_y \cdot \Gamma_z \quad (2-23)$$

For typical EELs,  $\Gamma_z$  and  $\Gamma_y$  approaches unity and  $\Gamma_x$  ranges from 3% to 15%. Due to different confinement effect and field size in the transverse plane, the output beam shows different divergence angles in x and y direction.

### General Characteristics of VCSELs

The operation of a VCSEL, like above descriptions, can be understood by analyzing the flow of carriers into active regions, the generation of photons due to the recombination of some of these carriers, and the transmission of some of these photons out of the laser cavity. Consider a generic VCSEL illustrated in Figure 2-5



with an active layer radius of  $a$  and active and effective cavity lengths of  $L_a$  and  $L$ , respectively. The threshold condition can be written as:

$$g_{th} = \alpha_a + \alpha_p \left( \frac{1}{\Gamma} - 1 \right) + \frac{1}{\Gamma \cdot L_a} \ln \left( \frac{1}{R_1 R_2} \right) + \alpha_d \quad (2-24)$$

where  $\alpha_a$  and  $\alpha_p$  are the absorption loss in the active and passive layers, respectively,  $R_1$  and  $R_2$  are the reflectivities of two mirrors, and  $\alpha_d$  is the diffraction loss. The confinement factor is expressed as the product of the longitudinal confinement factor  $\Gamma_z$  and the transverse factor  $\Gamma_{xy}$ , which is nearly unity for VCSELs. The longitudinal confinement factor  $\Gamma_z$  is expressed as:

$$\Gamma_z = \frac{L_a}{L} \cdot \xi \quad (2-25)$$

The last factor,  $\xi$ , is referred to as the axial enhancement factor, because it enhances the normally expected fill factor  $L_a/L$  in the axial confinement factor. When the field is approximated as a sinusoid enveloped by a decaying exponential in the DBRs,  $\xi$  reduces to [1, 2]

$$\xi = e^{-z_{DBR}/L_{DBR}} (1 + \cos(2\beta z_s)) \cdot \frac{\sin \beta L_a}{\beta L_a} \quad (2-26)$$

where  $\beta = 2\pi n_r/\lambda$  is the axial propagation constant,  $z_s$  is the shift between the active layer center and the standing-wave peak, and the exponential pre-factor accounts for placement of the active region within the DBR mirror. In this,  $z_{DBR}$  is the distance to the active material measured from the cavity-DBR interface and  $L_{DBR}$  is the penetration depth of optical energy into the DBR. If the active region is placed between the mirrors,  $z_{DBR}$  is zero, and the pre-factor is unity. If a thin active layer is centered on the standing-wave peak in the cavity,  $\xi$  can be as large as 2. If the active layer is thick enough,  $\xi$  is unity. If a thin active layer is placed at a null ( $2\beta z_s = \pi$ ),  $\xi$  can be near zero.

Table 2-1 lists the calculations of equation (2-8) and (2-24) for EEL and VCSEL threshold conditions, respectively. For VCSEL operations, the reflectivity,  $R$ , has to

be greater than 99.8% to reach threshold gain of  $0.1 \mu\text{m}^{-1}$ . In order to reduce the threshold gain, it's better to have smaller absorption in the passive layers. In addition, reducing the thickness of cladding layers and the penetration depths of DBRs are effective ways to lower the chance of absorption.

Typically, the cavity length of VCSELs is on the order of half operating wavelength. In such a short cavity device, the width of mode spacing is larger than the line-width of a typical semiconductor gain medium as shown in Figure 2-6. As a result, VCSEL operates with a single longitudinal mode. Since there's only one longitudinal mode within gain curve, the alignment between gain peak and cavity mode needs to be paid attention. Typically, the gain peak will red-shift as the temperature increases due to the band-gap shrinkage. At the same time, the cavity mode will also red-shift as the temperature increases due to the effective increase of the refractive index with the slower movement speed. Device engineers need to take into account the operation temperature to decide the best gain peak offset. Typically, for a commercial 850 VCSEL, the gain peak offset is set to be zero to few nanometers to assure proper operation during  $-10$  to  $85$  degree Celsius.

### **Transverse Modes in VCSELs**

Although VCSELs operate with single longitudinal mode, several transverse modes existed in VCSELs for typical aperture size ranging from  $5 \mu\text{m}$  to  $30 \mu\text{m}$  in diameter. Take a VCSEL with oxidized aperture for example shown in Figure 2-8. Due to the complex 3-D structure for oxide VCSEL, the analysis of transverse mode can be assumed an optical waveguide using effective index model [3]. The effective refractive index of core region can be calculated as  $n_1$ , while that of outer region is  $n_2$ . The simplest rule for single transverse mode operation is:

$$V_n = \frac{2\pi}{\lambda_o} \cdot a \cdot \sqrt{2 \cdot \Delta n \cdot n_1} < 2.405 \quad (2-27)$$

where

$$\frac{\Delta n}{n_1} = \frac{\Delta \lambda_o}{\lambda_o} \quad (2-28)$$

$$\Delta n = \frac{n_1 - n_2}{n_1} \quad (2-29)$$

and  $\lambda_o$  is the operating wavelength and  $V_n$  is the normalized frequency. The index difference of oxide VCSEL originates from the built-in oxidized layer with lower refractive index in comparison to periphery semiconductor materials. Due to the accurate position of oxidized aperture, tightly defining the injected carriers into the active regions and the built-in index guiding provided by the oxidized layer, the oxide-confined VCSELs have shown superior threshold current, efficiency and modulation speed in comparison to the proton implanted VCSELs [4]. However, the good transverse optical confinement results in multimode emission even in small aperture devices. Furthermore, the presence of the oxidized aperture and the inherent three-dimensional structure of the VCSEL have become a great challenge for researchers attempting to analyze and simulate the oxide-confined VCSELs [5]. Numerous works have been done in the study of the transverse emission mode patterns of the oxide-confined VCSELs to determine the mechanism of the transverse mode formation and evolution [6-12]. We report the investigation of the spontaneous emission patterns of oxide-confined VCSELs at the subthreshold condition using spectrally resolved near-field microscopy [13]. Figure 2-9 shows the example of transverse modes in oxide VCSELs. Not only the spontaneous emission patterns with similar mode structures as the stimulated emission patterns are observed, but also the high order Hermite-Gaussian and Laguerre-Gaussian modes are easily seen. We've also observed coexistence of two sets of identical lower order Hermite-Gaussian modes with different spot sizes, implying two cavity configurations in oxide-confined VCSELs and complex mechanism responsible for formation of laser modes in

oxide-confined VCSELs.

## 2-2 Modeling the Gain Mediums

### Optical Gain in Semiconductors

As shown in Figure 2-10, parabolic band structure approximation is used for conduction and valence band E-K relationship. The density of states for the combined system involving transition between  $E_2$  and  $E_1$  can be written as:

$$N_r(E) = \left(\frac{1}{2\pi^2}\right) \cdot \left(\frac{2m_r^*}{\hbar^2}\right)^{3/2} \cdot (h\nu - E_g)^{1/2} \quad (2-30)$$

where the reduced effective mass is:

$$\frac{1}{m_r^*} = \frac{1}{m_c^*} + \frac{1}{m_v^*} \quad (2-31)$$

$m_c^*$  and  $m_v^*$  is the effective mass for electron and hole, respectively, and  $h\nu$  is the emission photon energy.

Assumed:

- (1) The Einstein coefficient, B, is the same for semiconductor,
- (2) Photon energy density is  $\rho(\nu)d\nu = n_p \cdot h\nu$ , where  $n_p$  is the photon density,
- (3) Density of states is expressed as  $N_r(\nu)$ ,

The transition rate between  $E_2$  and  $E_1$  can be written as:

$$\text{➤ Stimulated absorption: } R_{1 \rightarrow 2} = B_{12} \rho(\nu) d\nu \cdot N_r(\nu) \cdot [f_v(E_1)(1 - f_c(E_2))] \quad (2-32)$$

$$\text{➤ Stimulated emission: } R_{2 \rightarrow 1} = B_{21} \rho(\nu) d\nu \cdot N_r(\nu) \cdot [f_c(E_2)(1 - f_v(E_1))] \quad (2-33)$$

The net stimulated emission rate is:

$$R_{st} = R_{2 \rightarrow 1} - R_{1 \rightarrow 2} = B \rho(\nu) d\nu \cdot (f_2 - f_1) \quad (2-34)$$

where

$$f_2 = \frac{1}{e^{(E_2 - E_{fc})/kT} + 1} = f_c(E_2), \quad f_1 = \frac{1}{e^{(E_2 - E_{fv})/kT} + 1} = f_v(E_1) \quad (2-35)$$

If  $f_2 - f_1 > 0$  or  $< 0$ , the stimulated emission or absorption occurs. If  $f_2 - f_1$  equals to zero, the transparent condition occurs. Thus, the condition for net stimulated emission

is:

$$E_g \leq E_2 - E_1 < E_{fc} - E_{fv} \quad (2-36)$$

The gain is defined as the ratio of net power emitted per unit volume over the power crossing per unit area. As shown in Figure 2-11, an incident light pass the distance of  $dz$  and gains the amount of power  $\Delta I$ . The speed of light is  $v_g$ , where  $dz = v_g * \Delta t$ . The power of light can be express as:  $I(\nu) = [\rho(\nu)d\nu]*v_g$ . The optical gain coefficient is written as:

$$\begin{aligned} \gamma(\nu) &= \frac{R_{st} \cdot h\nu}{\rho(\nu)d\nu \cdot v_g} \\ &= B\left(\frac{h\nu}{v_g}\right)N_r(\nu)(f_2 - f_1) \\ &= B\left(\frac{h\nu}{v_g}\right)hN_r(E)(f_2 - f_1) \quad (cm^{-1}) \end{aligned} \quad (2-37)$$

After the introduction to the concept of gain in a relative macroscopic point of view, the detail behavior and interaction between light and atomic system require quantum mechanical analysis. If we consider an atom with two-level energy system, the electron under light interaction has the Hamiltonian expressed by:

$$H = \frac{1}{2m}(\mathbf{p} + e\mathbf{A})^2 + V(r) \quad (2-38)$$

where  $\mathbf{A}$  is the vector potential. The above equation can be expanded as:

$$\begin{aligned} H &= \frac{\mathbf{p}^2}{2m} + \frac{e}{2m}[\mathbf{p} \cdot \mathbf{A} + \mathbf{A} \cdot \mathbf{p}] + \frac{e^2}{2m}\mathbf{A}^2 + V(r) \\ &= \left\{ \frac{\mathbf{p}^2}{2m} + V(r) \right\} + \left\{ \frac{e}{m}[\mathbf{A} \cdot \mathbf{p}] \right\} \\ &= H_o + H' \end{aligned} \quad (2-39)$$

The term,  $H'$ , can be viewed as a time-dependent perturbation to the original Hamiltonian,  $H_o$ . This perturbation term is the driving force for transitions between the conduction and valence bands. From solutions of time-dependent Schrodinger's

equation, the transition rate for semiconductors can be obtained as:

$$R_{21} = \frac{2\pi}{\hbar} |H'_{21}|^2 N_r(E_{21}) \delta(E_{21} - \hbar\omega) \quad (2-40)$$

where

$$H'_{21} = \int \varphi_2^* H' \varphi_1 d^3r = \langle 2 | H' | 1 \rangle \quad (2-41)$$

Equation (2-40) is known as Fermi's Golden Rules. Compared with equation (2-33) and (2-40), and substituted Einstein coefficient,  $B$ , with matrix element,  $|H'_{21}|$ , the gain expression can be rewritten as:

$$\gamma(\nu) = \frac{2\pi}{\hbar} \cdot |H'_{21}|^2 \cdot \left(\frac{1}{v_g n_{ph}}\right) \cdot N_r(E) \cdot (f_2 - f_1) \quad (2-42)$$

The matrix element,  $|H'_{21}|$ , determines the strength of interaction between two states. In semiconductors,  $\varphi_2$  and  $\varphi_1$  in equation (2-41) are expressed as:

$$\varphi_1 = F_1(r) * u_v(r) \quad \text{for valence band,} \quad (2-43)$$

$$\varphi_2 = F_2(r) * u_c(r) \quad \text{for conduction band,} \quad (2-44)$$

where:

- (1)  $u_v(r)$  and  $u_c(r)$  are Bloch functions of parabolic potential with atomic scale,
- (2)  $F_1(r)$  and  $F_2(r)$  are envelope functions of macroscopic potential, satisfying Schrodinger's equation in such as quantum wells, quantum dots. The bulk, quantum-well, and quantum-wire envelope functions take the following form:

$$F(r) = \frac{1}{\sqrt{V}} \cdot e^{jk \cdot r} \quad (\text{bulk}) \quad (2-45)$$

$$F(r) = \frac{1}{\sqrt{A}} \cdot e^{jk \cdot r_{\parallel}} \quad (\text{quantum well}) \quad (2-46)$$

$$F(r) = \frac{1}{\sqrt{L}} \cdot e^{jk_z \cdot z} \quad (\text{quantum wire}) \quad (2-47)$$

If we define:

$$\mathbf{A} = \frac{1}{2} [ |A_o(r)| e^{jk \cdot r} + |A_o(r)|^* e^{-jk \cdot r} ] \quad (2-48)$$

The  $H'$  can be written as:

$$H' = \frac{eA_o}{2m_o} (\hat{\mathbf{e}} \cdot \mathbf{p}) \quad (2-49)$$

Then,

$$\begin{aligned} H'_{21} &= \int \phi_2^* H' \phi_1 d^3 r \\ &= \frac{e}{2m_o} \int \phi_2^* (A_o \hat{\mathbf{e}} \cdot \mathbf{p}) \phi_1 d^3 r \\ &= \frac{e}{2m_o} \int F_2^* u_c^* (A_o \hat{\mathbf{e}} \cdot \mathbf{p}) F_1 u_v d^3 r \\ &= \frac{e}{2m_o} \left[ \int F_2^* u_c^* u_v (A_o \hat{\mathbf{e}} \cdot \mathbf{p}) F_1 d^3 r \Rightarrow (u_c^* u_v = 0), \right. \\ &\quad \left. + \int [F_2^* (A_o) F_1] [u_c^* (\hat{\mathbf{e}} \cdot \mathbf{p}) u_v] d^3 r \right] \\ &= \frac{eA_o}{2m_o} \int [F_2^* F_1] [u_c^* (\hat{\mathbf{e}} \cdot \mathbf{p}) u_v] d^3 r \\ &= \frac{eA_o}{2m_o} \underbrace{\langle u_c |}_{\text{Overlap of Bloch}} \underbrace{\hat{\mathbf{e}} \cdot \mathbf{p} / u_v \rangle}_{\text{Envelope function}} \underbrace{\langle F_2 | F_1 \rangle}_{\text{overlap integral}} \equiv \left( \frac{eA_o}{2m_o} \right) | \mathbf{M}_T | \end{aligned} \quad (2-50)$$

Overlap of Bloch function      Envelope function  
function      overlap integral

where  $|\mathbf{M}_T|$  is known as transition matrix element. Since photon energy density is  $n_{ph} \cdot h\nu$ , and electromagnetic wave energy density =  $1/2 \cdot n_r^2 \xi_o |E|^2$ , the  $A_o$  can be derived as:

$$\begin{aligned} E &= -j\omega A_o; \\ |E|^2 &= \omega^2 |A_o|^2; \\ n_{ph} \cdot h\nu &= \frac{1}{2} n_r^2 \cdot \epsilon_o \cdot \omega^2 |A_o|^2; \\ |A_o|^2 &= \left( \frac{2\hbar}{n_r^2 \epsilon_o \omega} \right) \cdot n_{ph} \end{aligned} \quad (2-51)$$

And the equation (2-42) can be rewritten as:

$$\begin{aligned} \gamma(\nu) &= \left( \frac{e^2 \hbar}{2\epsilon_o n_r c m_o^2 h \nu} \right) \cdot | \mathbf{M}_T | \cdot N_r(E) \cdot (f_2 - f_1) \\ &= \gamma_{\max} \cdot (f_2 - f_1) \end{aligned} \quad (2-52)$$

### Optical Gain in Quantum Well Structures

We specially pay attention to the optical gain for quantum well structures, since

the active mediums for all the devices in this study have quantum wells (QW). If we assume the potential confinement is along the  $z$  direction, the envelope function overlap integral can be expressed as:

$$\begin{aligned} \langle F_2 | F_1 \rangle &= \frac{1}{A} \int F_2^*(z) e^{jk_2 \cdot r_{\parallel}} F_1(z) e^{-jk_1 \cdot r_{\parallel}} d^3 r; \\ \text{for } k_2 &= k_1; \\ \langle F_2 | F_1 \rangle &= \frac{1}{A} \int F_2^*(z) \cdot F_1(z) dz \end{aligned} \quad (2-53)$$

Due to orthogonality between the quantum-well wave-function solutions, the overlap integral in equation (2-53) reduces to the following rule for sub-band transitions:

$$|\langle F_2 | F_1 \rangle|^2 \cong \delta_{n_c, n_v} \quad (2-54)$$

This means that transitions can only occur between quantum-well sub-bands which have the same quantum number,  $n_c = n_v$ . These are referred to as allowed transitions.

Transitions between sub-bands with dissimilar quantum numbers are forbidden transitions. Both are illustrated in Figure 2-12.

Except for the envelope function overlap integral; the other term in transition matrix element is the overlap of Bloch function, which is also known as momentum matrix element  $|\mathbf{M}|^2$ :

$$|\mathbf{M}_T|^2 = |\mathbf{M}|^2 \cdot |\langle F_2 | F_1 \rangle|^2 \quad (2-55)$$

The momentum matrix element, which is polarization dependent, determines the transition probability between conduction band and valence band. To further define the Bloch functions of the various energy bands, the corresponding atomic orbitals have to be taken into account. The Bloch function,  $u_s$ , corresponding to the isotropic  $s$  atomic orbital in conduction band remains the same. However, the Bloch functions  $u_x$ ,  $u_y$  and  $u_z$  corresponding to three  $p$  atomic orbitals for valence bands:  $p_x$ ,  $p_y$  and  $p_z$ , interact with each other along with the spin up and down. Using the  $kp$  theory, the modified valence bands are shown in Figure 2-13. The three valence bands are



commonly known as the heavy-hole (HH), light-hole (LH), and split-off hole (SO) bands. Since the constant  $|\mathbf{M}|^2$  can be determined experimentally, Table 2-2 has listed the reported values for several important materials. Table 2-3 summarizes the results for bulk and quantum-well materials for either transverse electric (TE: electric field in the quantum-well plane) or transverse magnetic (TM: electric field perpendicular to quantum-well plane) polarizations.

### Nonradiative Transitions

Nonradiative transition is relatively important when considering the overall carrier recombination process. Three major types of nonradiative transitions are depicted in Figure 2-14. The first type of nonradiative recombination happens when existing an energy level in the middle of the gap, which serves to trap an electron from the conduction band temporarily before releasing it to the valence band. Defects in the lattice structure are one source of traps. The recombination rate, also referred as Shockley-Read-Hall recombination, takes the form:

$$R_d = \frac{NP - N_i^2}{(N^* + N)\tau_h + (P^* + P)\tau_e} \quad (2-56)$$

where  $N_i$  is the intrinsic carrier concentration,  $\tau_e$  is the time required to capture an electron from the conduction band assuming all traps are empty,  $\tau_h$  is the time required to capture a hole from the valence band assuming all traps are full, and  $N^*$  and  $P^*$  are the electron and hole densities that would exist if the Fermi level was aligned with the energy level of the trap. For the laser applications, equation (2-56) can be simplified with the high-level injection regime:

$$R_d = \frac{N}{\tau_h + \tau_e} \quad (2-57)$$

The second type of nonradiative recombination in Figure 2-13 depicts electrons recombining via surface states of the crystal. The surface recombination rate under

$$R_s = \frac{a_s}{V} v_s N \quad 32$$

high level injection in the active region can be expressed as:

$$(2-58)$$

where  $a_s$  is the exposed surface area,  $V$  is the volume of the active region, and  $v_s$  is the surface recombination velocity. Surface recombination is most damaging when the exposed surface-to-volume ratio is large. In addition, devices when make use of regrowth technique can suffer from poor interfaces and hence high interface recombination. Surface recombination is also material dependent. The recombination velocity of short-wavelength GaAs system is one order greater than that of long-wavelength quaternary InGaAsP system.

The last type of nonradiative recombination depicted in Figure 2-14 is basically a collision between two electrons, which knocks one electron down to the valence band and the other to a higher energy state in the conduction band. An analogous collision can occur between two holes in the HH band and either SO or LH band. The above three types of collision are referred to as Auger processes. In laser applications with high injection level, the Auger recombination rate can be expressed as:

$$R_A = CN^3 \quad (2-59)$$

where  $C$  is a generic experimentally determined Auger coefficient. In long wavelength InGaAsP materials, the Auger coefficient is one order larger than GaAs systems since the smaller band-gap in InGaAsP materials enhances the probability of momentum conservation. The reduced material dimensionality, such as quantum well, appears to reduce the Auger process due to the modification of band structures. Another possible method of minimizing Auger recombination is to use strained materials in active layers.

### **Optical Gain in Strained Quantum Wells**

Strained QWs use a material, which has different native lattice constant than the

surrounding lattice constant. As shown in Figure 2-15, if the QWs native lattice constant is larger than the surrounding lattice constant, the QW lattice compress in the plane, and the lattice is said to be under compressive strain. If the opposite is true, the QW is under tensile strain. However, in any lattice-mismatched system, it is important to realize that there is a critical thickness beyond which the strained lattice will begin to revert back to its native state, causing high densities of lattice defects. For typical applications, this critical thickness is on the order of a few hundred angstroms, thus limiting the number of strained QWs in active layers.

Because the energy gap of a semiconductor is related to its lattice spacing, distortions in the crystal lattice should lead to alterations in the bandgap of the strained layer. There are two types of modifications. The first effect produces an upward shift in the conduction band as well as a downward shift in both valence bands, increasing the overall bandgap by an amount,  $H$  (which is positive for compressive strain and negative for tensile strain). The  $H$  indicates that this shift originate from the hydrostatic component of the strain. The second important effect separates the HH and LH bands, each being pushed in opposite directions from the center by an amount,  $S$ . The  $S$  indicates that this shift originates from the shear component of the strain. Figure 2-16 illustrates the energy shifts of the bands for biaxial strains. No only the energy shift, the band curvatures will be modified due to the strain effect. For a quantum-structure such as an  $\text{In}_{1-x}\text{Ga}_x\text{As}$  layer sandwiched between InP barriers, the band structures are shown in Figure 2-17 for (a) a compressive strain ( $x < 0.468$ ), (b) no strain ( $x = 0.468$ ), and (c) a tensile strain ( $x > 0.468$ ) [18]. The left-hand side shows the quantum-well band structures in real space vs. position along the growth ( $z$ ) direction. The right-hand side shows the quantized subband dispersions in momentum space along the parallel ( $k_x$ ) direction in the plane

of the layer. These dispersion curves show the modification of the effective masses or the densities of states due to both the quantization and strain effects.

The above characteristics provide some advantages in using strained materials over unstrained materials. First, the bandgap can be adjusted to obtain certain emission wavelength. Next, the reduction in hole masses leads to lower threshold lasing and lower Auger recombination rate. Then, the applied strain can allow laser emission with tailored polarization. Finally, the built-in strain may suppress defect migration into the active region. More detailed demonstrations of the strain effect will be given in chapter 4.

### 2-3 Characteristics of Distributed Bragg Reflectors

From the discussions in chapter 1, the high-reflectivity DBRs are extremely important components in VCSELs. In this section, we'd like to discuss the characteristics of DBRs. We start this section with the transfer matrix method in stacks of thin films. We construct a computational simulation program for the transfer matrix. Then, based on the simulation, we'll discuss the reflectance, transmittance, absorption, phase delay, and penetration depth for the DBRs.

#### Transfer Matrix Method

A thin film is shown in Figure 2-18(a) [19]. The direction of the incident wave is denoted by the symbol + (that is, positive-going) and waves in the opposite direction is – (that is, negative-going). Since there is no negative-going wave in the substrate and the waves in the film can be summed into one resultant positive-going wave and one resultant negative-going wave. At this interface  $b$ , then, the tangential components of  $E$  and  $H$  are:

$$\begin{aligned} E_b &= E_{1b}^+ + E_{1b}^- \\ H_b &= \eta_1 E_{1b}^+ - \eta_1 E_{1b}^- \end{aligned} \quad (2-60)$$

(2-61)

where  $\eta$  is the optical admittance of the film. Different polarizations have different forms:

$$\text{for s-polarization (TE): } \eta_s = n \cos \theta \sqrt{\epsilon_o / \mu_o} \quad (2-62)$$

$$\text{for p-polarization (TM): } \eta_s = n \sqrt{\epsilon_o / \mu_o} / \cos \theta \quad (2-63)$$

Hence

$$E_{1b}^+ = \frac{1}{2}(H_b / \eta_1 + E_b) \quad (2-64)$$

$$E_{1b}^- = \frac{1}{2}(-H_b / \eta_1 + E_b) \quad (2-65)$$

$$H_{1b}^+ = \eta_1 E_{1b}^+ = \frac{1}{2}(H_b + \eta_1 E_b) \quad (2-66)$$

$$H_{1b}^- = -\eta_1 E_{1b}^- = \frac{1}{2}(H_b - \eta_1 E_b) \quad (2-67)$$

The field at the other interface a at the same instant and at a point with identical  $x$  and  $y$  coordinates can be determined by altering the phase factors of the waves to allow for a shift in the  $z$  coordinate from 0 to  $-d$ . The phase factor of the positive-going wave will be multiplied by  $\exp(i\delta)$  where

$$\delta = 2\pi n_1 d \cos \theta_1 / \lambda \quad (2-68)$$

and  $\theta_1$  may be complex, while the negative-going phase factor will be multiplied by  $\exp(-i\delta)$ . There the values of  $E$  and  $H$  at the interface are:

$$E_{1a}^+ = E_{1b}^+ e^{i\delta} = \frac{1}{2}(H_b / \eta_1 + E_b) e^{i\delta}$$

$$E_{1a}^- = E_{1b}^- e^{-i\delta} = \frac{1}{2}(-H_b / \eta_1 + E_b) e^{-i\delta}$$

$$H_{1a}^+ = H_{1b}^+ e^{i\delta} = \frac{1}{2}(H_b + \eta_1 E_b) e^{i\delta}$$

$$H_{1a}^- = H_{1b}^- e^{-i\delta} = \frac{1}{2}(H_b - \eta_1 E_b) e^{-i\delta}$$

So that

$$E_a = E_{1a}^+ + E_{1a}^- = E_b \cos \delta + H_b \frac{i \sin \delta}{\eta_1}$$

$$H_a = H_{1a}^+ + H_{1a}^- = E_b i \eta_1 \sin \delta + H_b \cos \delta$$

This can be written in matrix notation as:

$$\begin{bmatrix} E_a \\ H_a \end{bmatrix} = \begin{bmatrix} \cos \delta & (i \sin \delta) / \eta_1 \\ i \eta_1 \sin \delta & \cos \delta \end{bmatrix} \begin{bmatrix} E_b \\ H_b \end{bmatrix} \quad (2-69)$$

The  $2 \times 2$  matrix on the right-hand side of equation (2-69) is known as the characteristic matrix of the thin film. Let another thin film be added to the single film so that the final interface is now denoted by c, as shown in Figure 2-18(b). The characteristic matrix of the film nearest the substrate is:

$$\begin{bmatrix} \cos \delta_2 & (i \sin \delta_2) / \eta_2 \\ i \eta_2 \sin \delta_2 & \cos \delta_2 \end{bmatrix}$$

And from equation (2-69):

$$\begin{bmatrix} E_b \\ H_b \end{bmatrix} = \begin{bmatrix} \cos \delta_2 & (i \sin \delta_2) / \eta_2 \\ i \eta_2 \sin \delta_2 & \cos \delta_2 \end{bmatrix} \begin{bmatrix} E_c \\ H_c \end{bmatrix}$$

and

$$\begin{bmatrix} E_a \\ H_a \end{bmatrix} = \begin{bmatrix} \cos \delta_1 & (i \sin \delta_1) / \eta_1 \\ i \eta_1 \sin \delta_1 & \cos \delta_1 \end{bmatrix} \begin{bmatrix} \cos \delta_2 & (i \sin \delta_2) / \eta_2 \\ i \eta_2 \sin \delta_2 & \cos \delta_2 \end{bmatrix} \begin{bmatrix} E_c \\ H_c \end{bmatrix}$$

If we define a characteristic matrix of the assembly, the above equation becomes:

$$\begin{bmatrix} B \\ C \end{bmatrix} = \begin{bmatrix} \cos \delta_1 & (i \sin \delta_1) / \eta_1 \\ i \eta_1 \sin \delta_1 & \cos \delta_1 \end{bmatrix} \begin{bmatrix} \cos \delta_2 & (i \sin \delta_2) / \eta_2 \\ i \eta_2 \sin \delta_2 & \cos \delta_2 \end{bmatrix} \begin{bmatrix} 1 \\ \eta_3 \end{bmatrix}$$

This result can be immediately extended to the general case of an assembly of  $q$  layers, when the characteristic matrix is simply the product of the individual matrices taken in the correct order, i.e.

$$\begin{bmatrix} B \\ C \end{bmatrix} = \left( \prod_{r=1}^q \begin{bmatrix} \cos \delta_r & (i \sin \delta_r) / \eta_r \\ i \eta_r \sin \delta_r & \cos \delta_r \end{bmatrix} \right) \begin{bmatrix} 1 \\ \eta_m \end{bmatrix}$$

(2-70)

where we have now used the suffix  $m$  to denote the substrate or exit medium. If  $\theta_o$ , the angle of incidence, is given, the values of  $\theta_r$  can be found from Snell's law. So the reflectance, transmittance and absorptance can be expressed as [19]:

$$R = \left( \frac{\eta_o B - C}{\eta_o B + C} \right) \left( \frac{\eta_o B - C}{\eta_o B + C} \right)^* \quad (2-71)$$

$$T = \frac{4\eta_o \operatorname{Re}(\eta_m)}{(\eta_o B + C)(\eta_o B + C)^*} \quad (2-72)$$

$$A = \frac{4\eta_o \operatorname{Re}(BC^* - \eta_m)}{(\eta_o B + C)(\eta_o B + C)^*} \quad (2-73)$$

The phase change on reflection can be expressed as:

$$\phi = \tan^{-1} \left( \frac{i\eta_o (CB^* - BC^*)}{i\eta_o^2 (BB^* - BC^*)} \right) \quad (2-74)$$

### Reflection Delay and Penetration Depth of DBRs

Since we are interesting in Bragg mirrors (quarter-wave mirrors) with incident light normal to the interfaces, the above equations can be much simplified. Due to the distributed nature of quarter-wave stack, these mirrors exhibit phase dispersion and a finite delay upon reflection [20]. The dispersion is responsible for pulse broadening and distortion [21], whereas the reflection delay adds to the laser cavity round-trip time. The storage of electromagnetic energy in a distributed reflector is also a factor of interest in the case of small-cavity structures where the cavity volume and the cavity round-trip time are of comparable magnitude as the mirror storage and the reflection delay. It has been common practice [22] to account for both the reflection delay time and the energy storage in distributed laser mirrors by defining a quantity called penetration depth as the depth inside the mirror at which the optical pulse appears to reflect, or the energy falls off to  $1/e$  of its initial value. The sum of the

physical cavity length and the mirror penetration depth gives the effective cavity length.

Figure 2-19 shows the simulation results of InGaAlAs/InAlAs DBRs with center wavelength at 1550 nm for 10, 20, 30 and 40 pairs. Figure 2-19(a), (b) and (c) demonstrate the reflectivity, phase and delay time, respectively. Figure 2-20 illustrates the interpretation of penetration depth: a wave is incident from a medium with refractive index  $n$  onto a DBR with linear phase. Its reflection is delayed by  $\tau$  and scaled by the value of the reflectivity. The equivalent model for the DBR is realized by extending the incident medium beyond the reference plane and by placing a fixed-phase mirror at depth  $L_{DBR}$ . To the observer placed to the left of the reference plane, the mirrors will appear equivalent if the reflectivity and the phase characteristics of the two cases are equal. The effective length and phase can be expressed as:

$$L_{DBR} = \frac{c\tau}{2n} \quad \theta_o = \omega_o\tau \quad (2-74)$$

where the reflection delay is:

$$\tau = -\frac{\partial\phi(\omega)}{\partial\omega} \quad (2-75)$$

and  $L_{DBR}$  is the penetration depth. Figure 2-21 shows the simulated electric field in a 40 pairs InGaAlAs/InAlAs DBRs. The intensity of the electric field decreases from the incident plane. The distance from the incident plane to  $1/e$  of the magnitude of the incident intensity represents the penetration depth. This depth needs to be considered in the determination of cavity mode wavelength in FP lasers and longitudinal confinement factor in VCSELs. The confinement factor is given by the ratio of electromagnetic energy in the active region of length  $L_a$  and the total energy present in the cavity:

$$\Gamma_L = \frac{L_a}{L_{FP} + 2L_{DBR}} \quad (2-76)$$



From equation (2-76), the longer penetration depth will lower the confinement factor. If the absorption is taken into account, the longer traveling path will increase more loss. Table 2-4 lists various kinds of material combination for making DBRs with center wavelength at 1550 nm. The larger refractive index difference between the DBR layers leads to a smaller number of pairs to reach 99.9% reflectivity and a shorter penetration depth.

## 2-4 Analysis of the Heat Flow

It is well known that the heating effect is very important for semiconductor lasers in almost all applications. For VCSELs with relatively small device volume, the heat dissipation is one of the major limitations for continuous-wave (CW) operations. Long wavelength VCSELs especially suffer from the temperature effect due to the insufficient gain at high temperature. We'd like to develop a thermal model by using finite element analysis (FEA) software to simulate the heat flow in VCSELs.

Typically, the VCSEL structure is cylindrical symmetry. The coordinates in thermal model can be transformed to longitudinal,  $z$ , and axial,  $r$ , directions. The input parameters for the thermal model include the geometry, the thermal conductivity  $k(T, r, z)$  of the materials, and the heat source distribution  $P(r, z)$ . The heat sources mainly originate from the Joule heat in conducting materials, nonradiative recombination and absorptions in active layers. The heat-transferred modal for the cylindrical symmetry can be expressed as:

$$\frac{\partial}{\partial r} k_r \frac{\partial T}{\partial r} + \frac{1}{r} k_r \frac{\partial T}{\partial r} + \frac{\partial}{\partial z} k_z \frac{\partial T}{\partial z} = - \frac{\partial P}{\partial V}(r, z) \quad (2-77)$$

where  $T$  is temperature and  $\partial P/\partial V$  is the heat power density. If we assumed anisotropic thermal conductivity in DBR layers, then:

$$k_r = \frac{d_1 k_1 + d_2 k_2}{d_1 + d_2} \quad \text{and} \quad k_z = \frac{d_1 + d_2}{d_1 / k_1 + d_2 / k_2}$$

(2-78)

where  $k_1$  and  $k_2$  are thermal conductivities for bulk materials and  $d_1$  and  $d_2$  are the DBR layer thicknesses. The partial differential equation (2-77) can be easily solved by FEA software [23]. The visualized outputs contain the temperature distribution and heat flow. The thermal resistance can be calculated from the temperature distribution  $T(r, z)$  with uniform heat source in the active region:

$$R_{th} = \Delta T_{max} / P_{heat} \quad (2-79)$$

Although heat flow in a VCSEL can be solved with the FEA software, the average device temperature can be easily evaluated. The power dissipated in the laser is

$$P_D = P_{in} - P_O = P_{in} (1 - \eta) \quad (2-80)$$

where  $\eta$  is the wall-plug efficiency, which is the ratio between the emitted optical power over the injected electrical power. Then, the temperature rise is:

$$\Delta T = P_D Z_T \quad (2-81)$$

where  $Z_T$  is the thermal impedance. For small VCSELs on a relatively thick substrate, a simple analytic expression for  $Z_T$  is useful [24]:

$$Z_T = \frac{1}{4k_T a_{eff}} \quad (2-82)$$

where  $k_T$  is the thermal conductivity of the substrate beneath the heat generating disk, and  $a_{eff}$  is the effective device radius. In the uncovered etched-mesa case,  $a_{eff}$  is approximately equal to the radius of active region; in other cases it tends to be somewhat larger due to heat spreading in either surrounding epitaxial material or deposited heat spreaders. In contrast, if the VCSEL is flip-chip bonded to a heat sink, a quasi-one-dimensional heat flow results, and then

$$Z_T = \frac{h}{k_T A} \quad (2-83)$$

where  $A$  is the effective area of the heat flow,  $h$  is the distance to the heat sink and  $k_T$  is the thermal conductivity of the material between the source and heat sink.

## 2-5 LW-VCSEL Designs

The fundamental issues in designing LW-VCSELs fall into four main categories: optical, gain, electrical and thermal considerations. First, in considerations of optical elements in LW-VCSEL, how to fabricate both mirrors with high reflectivity, large stop-band width and short penetration depth is important. The choices of materials for DBRs will influence the structure and the fabrication methods of VCSELs. In order to fabricate an efficient device, the optical confinement in transverse plane is necessary. In GaAs-based VCSELs, the oxidized high Al-contained aperture has been successfully applied to provide not only the optical confinement in transverse plane but also the precision current path to the active region, which makes good overlapping between optical field and carrier distributions. Unless the LW-VCSELs are made by wafer-fusion, in which the AlGaAs DBRs can be integrated with InP-based active region, other kinds of mechanisms for optical confinement in transverse plane have to be figured out. Buried tunnel junction [25] and under-cut active layer [26] have been successfully demonstrated.

Second, due to the stringent requirement in fiber communication, the LW-VCSELs have to be operated at 85°C with high-modulated speed. To improve the high temperature characteristics, it is effective using the materials in active region with large conduction-band offset, which can reduce the probability of hot electrons jumping over the barrier potential. The strained materials discussed above are also effective for increasing the high temperature characteristics since the reduction of threshold current and probability of Auger recombination. Strained multiple quantum

wells can help to improve the high temperature characteristics and high-speed modulation due to the increase of the differential gain. However, the number of strained multiple quantum wells cannot be too large. The strained field can be built-up while the number of strained multiple quantum wells increases to produce defects. Some groups had proposed strain-compensating multiple quantum wells to lessen the defect showing up. In addition, too many quantum wells in VCSEL cavity will reduce the longitudinal enhancement factor. The extra quantum wells will not provide more gain in laser operation but will increase the chance of absorption loss.

In electrical considerations, it's very important to efficiently transport the carriers into the effective active regions if there's an accurate definition of carrier path. Ion-implantation, oxidized aperture, buried-tunnel-junction [25] and under-cut [26] aperture have been successfully applied in VCSELs. Low serial resistance is also crucial in LW-VCSEL continuous-wave operations while low capacitance structure leads to high modulation speed. The major challenge in early VCSEL development is the relatively high serial resistance in p-type DBR. The resolution is to use the parabolic graded interface and modulation doping at the interfaces where are nodes of the standing wave field in VCSEL cavity.

The last issue is the thermal consideration in LW-VCSELs. Since the gain materials for long-wavelength range are sensitive to the high temperature, how to design a efficient device with low thermal resistance is rather important. As far as the materials are concerned, the dielectric mirrors are usually not good thermal conductors. In alloy system, the thermal conductance for binary compound is better than ternary compound; and ternary is better than quaternary. Flip-chip bonding can provide more direct heat dissipation path to the heat sink.

In addition to the above concerns, the single mode and low chirping operations

are important issues in optical communications. The reliability assurance and the capability of mass-production are also critical factors when designing LW-VCSELs. However, the one consideration in any category will influence or induce other considerations in other categories. As shown in Figure 2-22, the designing considerations influence with each other. For example, the DBRs made by InP-airgap demonstrate extremely high reflectivity, large stop-band width and short penetration depth in optical considerations. However, in electrical and thermal considerations, the InP-airgap DBRs are electrically and thermally insulating in longitudinal direction. Other kinds of design have to be adopted. For another example, the ion-implantation is an easy and mature technique to define current aperture in VCSEL structure. However, the ion-implanted aperture cannot provide good optical confinement in transverse plane. All in all, to successfully design and fabricate the LW-VCSELs, not only will every issue require optimization, all considerations related to each other require thorough optimizations.



## References

- [1] R. H. Yan, Z. M. Chuang, S. W. Corzine, and L. A. Coldren, *J. Appl. Phys.*, v67, p4387, 1990.
- [2] E. R. Hegblom, D. I. Babic, B. J. Thibeault, and L. A. Coldren, *IEEE J. Sel. Topics Quantum Electron.*, v3, p379, 1997.
- [3] G. R. Hadley, *Optics Lett.*, v20, no.13, p1483, 1995.
- [4] K. L. Lear, R. P. Schneider, Jr., K. D. Choquette, and S. P. Kilcoyne, *IEEE Photonics Technol. Lett.*, v8, p740, 1996.
- [5] J. S. Gustavsson, J. A. Vukusic, J. B. Bengtsson, and A. Larsson, *IEEE J. Quantum Electron.* v38, p203, 2002.
- [6] C. Degen, I. Fischer and W. Elsaber, *Optics Express*, v5, p38, 1999.
- [7] C. J. Chang-Hasnain, M. Orenstein, A V. Lehmen, L. T. Florez, J. P. Harbison, and N. G. Stoffel, *Appl. Phys. Lett.* v57, p218, 1990.
- [8] L. Raddatz, I. H. White, H. D. Summers, K. H. Hahn, M. R. Tan, and S.-Y. Wang, *IEEE Photonics Technol. Lett.*, v8, p743, 1996.
- [9] I. Horsch, R. Kusche, O. Marti, B. Weigl, and K. J. Ebeling, *J. Appl. Phys.*, v79, p3831, 1996.
- [10] J. Kim, D. E. Pride, J. T. Boyd, and H. E. Jackson, *Appl. Phys. Lett.*, v72, p3112, 1998.
- [11] J. Kim, J. T. Boyd, H. E. Jackson, and K. D. Choquette, *Appl. Phys. Lett.*, v76, p526, 2000.
- [12] W. C. Bradford, J. D. Beach, R. T. Collins, D. W. Kisker, and D. Galt, *Appl. Phys. Lett.*, v80, p929, 2002.
- [13] T. C. Lu, W. C. Hsu, Y. S. Chang, H. C. Kuo and S. C. Wang, manuscript submitted to *J. Appl. Phys.* and under revision, 2004.
- [14] C. Hermann and C. Weisbuch, *Phys. Rev. B*, v15, p823, 1977.
- [15] C. Hermann and C. Weisbuch, *Modern Problems in Condensed Matter Sciences Volume 8; Optical Orientation*, ed. V. M. Agranovich and A.A. Maradudin, North-Holland Co., p463, 1984.
- [16] B. Jani, P. Gilbert, J. C. Portal, and R. L. Aulombard, *J. Appl. Phys.*, v58, p3481, 1985.
- [17] R. J. Nicholas, J. C. Portal, C. Houlbert, P. Perrier, and T. P. Pearsall, *Appl. Phys. Lett.*, v34, p492, 1979.

- [18] S. L. Chuang, “*Semiconductor Lasers*” in *Physics of Optoelectronic Devices*, John Wiley and Sons, Inc, p443, 1995.
- [19] H. A. Macleod, “*Basic theory*” in *Thin-Film Optical Filters*, 2<sup>nd</sup> ed. McGraw-Hill, p35, 1989.
- [20] D. I. Babic and S. W. Corzine, *IEEE J. Quantum Electron.*, v28, no.2, p514, 1992.
- [21] P. Laporta and V. Magni, *Appl. Opt.* , v24, p2014, 1985.
- [22] F. Koyama, Y. Suematsu, S. Arai, and T. Tawee, *IEEE J. Quantum Electron.*, vQE-19, p1042, 1983.
- [23] *Partial Differential Equation Toolbox User’s Guide*, The MathWorks, Inc., p2-57, 1996
- [24] S. S. Kutateladze and V. M. Borishanski, *A Concise Encyclopedia of Heat Transfer*, Permagon, Oxford, 1966.
- [25] M. Ortsiefer, R. Shau, G. Bohm, F. Kohler, and M.-C. Amann, *Appl. Phys. Lett.*, v76, no.16, p2179, 2000.
- [26] E. Hall, S. Nakagawa, G. Almuneau, J.K. Kim and L.A. Coldren, *Electron. Lett.*, v36, no.17, p1465, 2000



**Table 2-1** Comparison of threshold conditions for EEL vs VCSEL.

	<i>EEL</i>	<i>VCSEL</i>
Active length, $L_a$	300 $\mu\text{m}$	0.01 $\mu\text{m}$
Confinement factor, $\Gamma$	0.03	1 (or 2)
$1/\Gamma L_a$	1/9 $\mu\text{m}^{-1}$	1/0.01 $\mu\text{m}^{-1}$
Mirror loss, $\ln(1/R)$	1.2 ( $R \sim 0.3$ )	0.001 ( $R \sim 0.998$ )
Threshold gain, $g_{th}$	0.1 $\mu\text{m}^{-1}$	0.1 $\mu\text{m}^{-1}$





**Table 2-2** Magnitude of  $|M|^2$  for various material systems.

<i>Material systems</i>	<i><math>2 M ^2/m_0</math> in eV</i>	<i>Reference</i>
GaAs	$28.8 \pm 0.15$	[14, 15]
$\text{Al}_x\text{Ga}_{1-x}\text{As}$ ( $x < 0.3$ )	$29.83+2.85x$	[16]
$\text{In}_x\text{Ga}_{1-x}\text{As}$	$28.8-6.6x$	[14, 15]
InP	$19.7 \pm 0.6$	[14, 15]
$\text{In}_{1-x}\text{Ga}_x\text{As}_y\text{P}_{1-y}$ ( $x=0.47y$ )	$19.7+5.6y$	[15, 17]



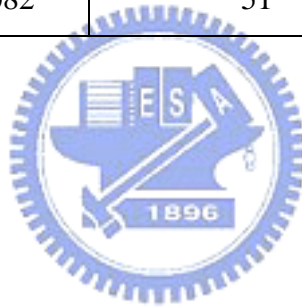
**Table 2-3** Magnitude of  $|\mathbf{M}_T|^2/|\mathbf{M}|^2$  for different transitions and polarizations. C-HH represents the transition from electron band to heavy hole band. C-LH represents the transition from electron band to light hole band

Polarization	Quantum-well			
	Bulk		$(k_t \sim 0)$	
	C-HH	C-LH	C-HH	C-LH
TE	1/3	1/3	1/2	1/6
TM	1/3	1/3	0	2/3



**Table 2-4** Various material combinations for making high reflectivity DBRs

DBR materials	$n/n_0$	Required pairs to reach $R > 99.9\%$	Penetration depth ( $L_{DBR}$ )
InP/Air	1.038	4	0.11 $\mu\text{m}$
TiO <sub>2</sub> /SiO <sub>2</sub>	0.509	7	0.14 $\mu\text{m}$
GaAs/AlAs	0.153	27	0.79 $\mu\text{m}$
AlGaAsSb/AlAsSb	0.149	28	0.87 $\mu\text{m}$
InGaAlAs/InP	0.102	41	1.26 $\mu\text{m}$
InGaAlAs/InAlAs	0.090	47	1.45 $\mu\text{m}$
INGaAsP/InP	0.082	51	1.59 $\mu\text{m}$

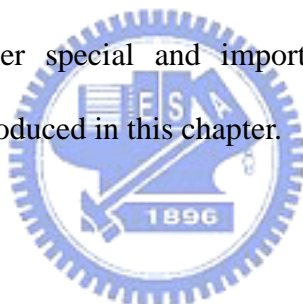


## CHAPTER 3

### Fabrication of Long Wavelength Vertical Cavity Surface

#### Emitting Lasers

This chapter mainly describes the fabrication equipments and procedures for long wavelength vertical cavity surface emitting lasers (LW-VCSELs). Metal organic chemical vapor deposition (MOCVD) system is used for growing all the epitaxial structures through out this study. Since the epitaxial equipment and process determine most of the characteristics of LW-VCSELs, detailed descriptions and specific functions of this MOCVD system are given in this chapter. The growth process, regrowth process and in-situ monitoring will also be addressed. Wafer fusion technique, which is the other special and important process in fabrication of LW-VCSELs, will also be introduced in this chapter.



#### 3-1 Metal Organic Chemical Vapor Deposition System

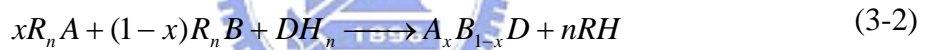
##### Reaction Equations

The MOCVD process for the growth of compound semiconductor materials and devices originated in the pioneering work of H. M. Manasevit [1]. This process is also called organometallic chemical vapor deposition (OMCVD), metalorganic vapor phase epitaxy (MOVPE), and organometallic vapor phase epitaxy (OMVPE). The simplest case in MOCVD [1] involves a pyrolysis reaction of the vapors of a volatile organometallic compound and a gaseous hydride, given by:

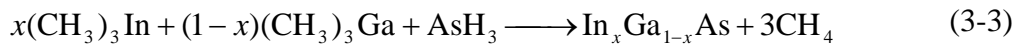


where  $R$  is an organic radical of some unspecified form but generally of lower order, such as a methyl- or ethyl-radical, and  $A$  and  $D$  are the constituent species for the

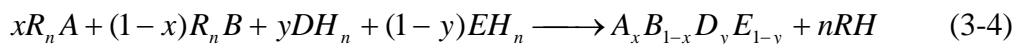
deposited solid. Many organometallic compounds have been studied as sources for the MOCVD processes, with the most important being trimethylgallium (TMGa), trimethylaluminum (TMAI), and trimethylindium (TMIn). In general, the organometallic constituents are transported to a heated substrate by passing a carrier gas, usually hydrogen, over or through the compound contained in a constant-temperature bubbler vessel. Most MOCVD growth of III-V compound semiconductors and alloys involves the use of hydrides, such as arsine or phosphine, for the column V species. In principle, these are the simplest of column V sources to use because they are already gaseous and supplied from simple cylinder-based delivery systems. The growth of semiconductor alloys by MOCVD is easily accomplished by mixing the vapors from the different alloy constituents in the appropriate vapor phase ratio to form the desired composition. A general equation for a ternary alloy is given by:



which applies, for example, to ternary InGaAs



A general equation for a quaternary alloy is given by

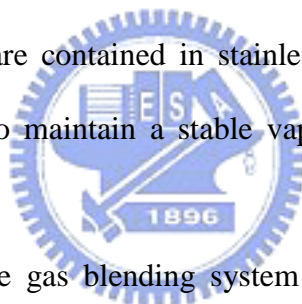


### Gas Blending Systems

Generally, there are four major components in the modern MOCVD system as shown in Figure 3-1: the gas blending unit, the reactor chamber, the vacuum system and the scrubbing system, all controlled by a programming logical unit. Figure 3-2 describes the basic function of these components. The gas blending unit is responsible for transporting and mixing the precursors. The reactor chamber with a heated susceptor determines the crystal quality, the layer thickness, and the uniformity. The

vacuum system is responsible for exhausting the gas after reaction and balancing the pressure in reactor chamber. The scrubbing system deals with the toxic gas after reaction for the safety considerations. The MOCVD system used in this study is D180 series manufactured by EMCORE Co. Ltd (now with Veeco Instruments). The gas blending system is illustrated in Figure 3-3.

The gas blending system [2-6] for D180 MOCVD system is a very clean, leak-free network of stainless-steel tubing, automatic valves, and electronic mass flow controllers. The carrier gas, hydrogen, is purified with the Palladium cell. Hydride delivering modules generally require a few valves and an electronic mass flow controller, since these sources are already provided as dilute, high pressure gases in gas cylinders. Alkyl delivery modules are more complicated. These high-vapor-pressure sources are contained in stainless-steel bubblers and held in a temperature-controlled bath to maintain a stable vapor pressure over the liquid or solid source.



An important part of the gas blending system is the supply of carrier gases within a vent-run configuration, shown in Figure 3-3 as the injection block. The design of the injection block can avoid transients from switching or dead space. The vent-run valves couple the individual source modules to the supply line. The stable and controllable source flow rate can then be established and stabilized while the valve is vented to a waste line and prior to injection into the run supply line as shown in Figure 3-3.

### **Reactor Chamber**

The reactor chamber is the vessel in which the source gases are mixed, introduced into a heated zone where an appropriate substrate is located, and the basic pyrolysis reactions take place. The reactor geometry in D180 MOCVD system is the

vertical type chamber as shown in Figure 3-4. The alkyl and hydride sources inject into the reactor via regulated mass flow controllers. The flow rate ratio between mass flow controllers labeled 1 to 3 for alkyl injection determines the growth rate and the uniformity of the epitaxial layers. Alkyl and hydride sources do not mix together until they reach the wafer surface in order to prevent the pre-reaction. The wafer carrier for D-180 type MOCVD contains six two-inch wafer recesses and is driven by the susceptor with high rotation speed. The reactor pressure for the epitaxial growth maintains at 70 torr controlled by the throttle valve. To achieve uniformly laminar gas flow near the wafer surface at relatively low pressure, the rotation speed is 900 round per minute. Two-zone heater locating just beneath the susceptor serves the heating source of the reactor. Adjusting the heating temperature settings of inner and outer filaments can modify the temperature distribution along the wafer surface.



### **Uniformity Issue**

The uniformity of the epitaxial layer in terms of thickness, composition and dopant concentration is very important for the MOCVD growth. Except for the reactor pressure, total gas flow rate, the rotation speed of the wafer carrier, two adjustable parameters in D180 type MOCVD system will influence the uniformity issues. The first parameter is the ratio between the settings of alkyl-injection mass flow controllers. This ratio determines the basic growth rate distribution across the entire wafer surface. A simple examination can be done is to grow a stack of DBRs and measure its peak reflectance distribution. Figure 3-5 shows examples grown in D180 type MOCVD reactor with different ratios between the settings of alkyl-injection mass flow controllers. The standard deviation for the peak reflectance can be obtained as small as 0.57% suggesting the growth rate across the entire wafer is only 0.57% in deviation. The second parameter is the ratio between the temperature

settings of inner and outer filaments. Limited to the configuration of high-speed rotation disk, however, temperature uniformity over the entire wafer surface is quite difficult to achieve. The heat is carried away mainly from the spindle by conduction and from the carrier gas by convection. Two-zone heating helps to adjust the temperature profile over the wafer surface. The temperature deviation over 20°C can be observed with the compositional differences over the wafer by measuring the X-ray peak or photoluminescence peak distributions. However, The temperature deviation smaller than 10°C is not easy to observe. The empirical solution is to correlate the characteristics of the optoelectronic devices, such as the slope efficiency of the laser diode, to the temperature distribution.

### **In-situ Monitoring**

The in-situ monitoring is very useful for growing optoelectronic devices such as VCSELs due to the stringent requirement of phase matching. The laser reflectometry is applied as the in-situ monitoring in D180 type MOCVD system. The schematic of configuration is shown in Figure 3-6(a). Two optical heads are mounted on the top flow flange of the reactor and monitoring the growth conditions for the upper and lower points of the wafer surface. An optical head couples two fibers; one is from the laser source with the emission wavelength at 905 nm, and the other is to the detector. By collecting the reflection of a 905 nm laser light perpendicularly impinging on the wafer surface, the growth rate can be obtain by

$$GR = \lambda T_d / 2n \quad (3-5)$$

where  $\lambda$  is 905 nm,  $T_d$  is the oscillation period of the reflectivity curve,  $n$  is the refractive index of the epitaxial layer at the growth temperature. It's very convenient to grow calibrated layer with  $5\lambda/4n$  thickness before the thick DBR is grown. Figure 3-6(b) shows the example for the measured reflectivity of a DBR structure. The use



of  $5\lambda/4n$  thickness in calibration layers will not interfere the phase conditions in DBR layers. The accurate growth rate of the DBR layers can be obtained and modified first by observing the calibration layers. Not only the growth rate can be monitored with this technique, but also the crystal quality can be monitored. If the average reflectivity value tends to decrease, the wafer surface becomes rough. It is better to stop the growth and check the growth parameters.

### 3-2 Epitaxial Regrowth Techniques

The regrowth technique has been used for fabricating optoelectronic devices with special purposes. “Regrowth” means the second or third epitaxial growth on the processed epitaxial structures. The surface conditions of the processed epitaxial structures have been different from the flat substrates. The cleanness of the wafer surface has to be taken care with special surface treatment before the regrowth. Different growth conditions have to be developed for the rugged surface after the lithography and etching processes. We have demonstrated several regrowth techniques for different devices with special functions [8, 9]. In this section, the parameters will be discussed for regrowth of InP-based devices. Typical processes for buried heterojunction (BH) lasers are shown in Figure 3-7. The surface of the regrowth layer is related to the etching conditions of the SiO<sub>2</sub> mask. The experiments showed that the lower of the dry etching power led to the better surface. The remnant SiO<sub>2</sub> carried by the high energy ions deep into the epitaxial layer was attributed to degrade the epitaxial surface as shown in Figure 3-8(a). Pictures in Figure 3-8 are taken by the field emission scanning electron microscope (SEM). The rabbit-ear phenomenon around the ridge has been discussed in literature [10]. We have applied two methods to obtain smooth regrowth surface around the ridge. One is to use pulse

mode growth [11] to increase the In migration time. The other is to increase the growth temperature to wet the rugged surface with the ridge structure. The smooth regrowth profile is shown in Figure 3-8(b)

### **3-3 Wafer Fusion Techniques**

Wafer fusion refers to a process by which two mirror-polished wafer adhere to each other without the application of any macroscopic gluing layer or outside force. Wafer fusion is alternatively known as “direct bonding.” In most cases, the wafer involved in actual applications are typical semiconductor wafers consisting of single-crystalline materials used in micro- or optoelectronics.

When two atomically smooth and clean surfaces are brought into intimate contact, they adhere to each other via intermolecular forces such as van der Waals forces or hydrogen bonding. By temperature treatment or introducing some monolayers of appropriate molecules into the interlayer, the bonding strength can be increased in such a way that it is comparable with the chemical bond and acts like a welding. Solids of almost any material combination may be joined through this room temperature technique.

The technique of wafer fusion is a viable processing method to combine semiconductor materials with different lattice constants. It removes the limitation to lattice matched materials given by epitaxial growth techniques and opens a new degree of freedom for the design of semiconductor device. In contrast to similar techniques, such as epitaxial lift off or silicon/silicon dioxide bonding, wafer fusion does not involve any foreign material at the interface. Instead, both materials are directly joined together and covalent bonds are formed on either side of wafer-fused heterojunctions, which are very similar to those of epitaxially grown interfaces. This

enables the fabrication of novel devices such as the silicon heterointerface photodetector [12, 13], wafer-fused vertical cavity lasers (VCSELs) [14, 15], resonant cavity photodetectors [16], or transparent substrate light emitting diodes [17, 18].

### **Introduction to Fusion Methods**

Several kinds of wafer bonding techniques have been developed. According to the bonds that formed at adhered interface, we can classify and list as follows.

#### **(1) Bonding by atomic rearrangement [19]**

Two wafers were put face to face and a molybdenum block was put on the top of the wafer to assure a close contact of the wafers. The sample was heated to 650°C and held at that temperature for 30 min with a hydrogen flow to remove the native oxide. After the desorption of native oxide, surface reconstruction takes place on two wafer surfaces to reduce the surface energy. When two surfaces are close enough, new chemical bonds are formed.

#### **(2) Van der Waals bonding [20]**

The method utilizes the formation of Van der Waals bond between surfaces of two wafers. After the clean process, proper thin de-ionized (D.I.) water films were left on two wafers. Two wafers were put face to face and a pressure was applied on the wafers. After all the D.I. water between two wafers disappeared, the two wafers were adhered together.

#### **(3) Surface activated bonding [21]**

The surfaces to be bonded are cleaned by sputtering and activated by argon fast

atom beam bombardment and then brought into contact with each other in an ultrahigh vacuum at room temperature. The sample was then annealed at low temperature.

### **Key Issues in Wafer Fusion Process**

One of the common problems associated with wafer fusion is the occurrence of unbonded interface areas which are frequently termed “interface bubbles” or “voids.” The unbonded area at the interface will degrade the electrical and optical characteristics of devices. The causes of unbonded area include:

- (1) Smoothness of wafer surface: Unsmooth wafer surface will induce the formation of unbonded areas causing voids and defects at the fusion interface [22].
- (2) Particles on wafer surface: Particles on wafer surface will cause the formation of bubbles or tent-like structure at fusion interface.
- (3) Uniform pressure: During fusion process, pressure is applied on wafers to make the atoms on the wafers surface contact to each other and form chemical bonds. Nonuniform pressure might cause nonuniform fused areas or even un-fused areas at the fusion interface.

### **Wafer Fusion System**

The main wafer fusion mechanism in this thesis is similar to “bonding by atomic rearrangement.” A fixture has been designed to press the wafers together at elevated temperatures. As illustrated in Figure 3-9, the fixture consists of two graphite plates with a diameter of 18 mm and two stainless discs with a diameter of 35 mm. Three pairs of molybdenum screws and screw nuts are used to fix the whole fixture. Thus, when heated, the wafer pair loaded inside was under a strong compression due to the large difference in linear thermal expansion of graphite, stainless and molybdenum,

which are  $9 \times 10^{-6} \text{K}^{-1}$ ,  $16 \times 10^{-6} \text{K}^{-1}$  and  $5.27 \times 10^{-6} \text{K}^{-1}$ , respectively. The compression can further force the two wafer surface to conform to each other and achieve a very close contact over the entire surface, even though the two original surfaces may have slight bowing or warps. As the two materials contact to each other in pressure and high temperature condition, the chemical bonds form at the interface and the two wafers fused together. Figure 3-10 is the apparatus of the wafer fusion system. The fusion chamber is made by stainless tube, which is located inside the 50 cm long furnace. The temperature of the furnace is controlled by a proportional integral derivative controller. The fusion chamber is pumped down and purged with  $\text{N}_2$ .

### **Preliminary Experiments for Fusion System Test**

In a long wavelength VCSEL fabricated with wafer fusion technique, the two materials bonded together at the interface are typically InP and GaAs. As the whole wafer fusion system was established, we first carried out the fundamental and preliminary experiments to examine the the fusion system and process.

The wafers used in this work are mirror-polished (100)  $0^\circ$  off GaAs and the InP substrates. First the wafers were cleaved into  $10 \times 12 \text{ mm}^2$ . The non-square geometry was chosen as means for recognizing the crystallographic orientation of the samples. Then the wafers were cleaned with acetone in ultra-sonic vibrator. After rinsing the wafers in de-ionized water, the mirror-polished surfaces were brought into contact with the (100) orientation of wafers aligned in de-ionized water and subsequently dried with  $\text{N}_2$ . The sample was put into the fusion fixture depicted in Figure 3-9. Then, the fixture was put into the fusion chamber. The fusion process was carried out in the fusion chamber with the furnace temperature at  $600^\circ\text{C}$  in  $\text{H}_2$  atmosphere for one hour. After fusion process, the two wafers were bonded to each other. The smple were cleaved into pecies to check the cross-section of the fusion interface. We observed

that the fused InP and GaAs wafer don't separate after cleave treatment indicating the well strength existing between the fusion interfaces.

Figure3-11 (a) and (b) show the optical microscope (OM) picture and SEM image of the cross-section of the cleaved interface respectively. From rudimentary observation of these pictures, the bonding interface is very smooth. The stripes on InP side might be caused by the cleavage process when the small different crystallographic orientation between InP and GaAs presented.

In summary, we have established the direct wafer fusion system and process. Reliable fusion mechanical intensity and smooth fusion interface between GaAs/InP provide good basement for further fabrication of LW-VCSELs.



## References

- [1] H. M. Manasevit, *Appl. Phys. Lett.*, v12, no.4, p156, 1968.
- [2] C. C. Wang and S. H. McFarlane, III, *J. Cryst. Growth*, v13/14, p262, 1972.
- [3] R. D. Dupuis, L. A. Moudy, and P. D. Dapkus, in *Inst. Phys. Conf. Ser.*, no.45, ch.1, p1–9, 1978,
- [4] E. J. Thrush, J. E. A. Whiteaway, and G. Wale-Evans, *J. Cryst. Growth*, v68, p412, 1984.
- [5] J. S. Roberts and N. J. Mason, *J. Cryst. Growth*, v68, p422, 1984.
- [6] H. Kawai, I. Hase, K. Kaneko, and N. Watanabe, *J. Cryst. Growth*, v68, p406, 1984.
- [7] M. R. Leys, C. Van Opdorp, M. P. A. Vieggers, and H. J. Talen-Van der Mheen, *J. Cryst. Growth*, v68, p431, 1984.
- [8] T.C. Lu, H. M. Shieh, and S.C. Wang, *Appl. Phys. Lett.* v80, no.11, p1882, 2002.
- [9] T.C. Lu, Richard Fu, H. M. Shieh, K. J. Huang, and S. C. Wang, *Appl. Phys. Lett.* v78, no.7, p853, 2001.
- [10] J. L. Zilko, B. P. Segner, U. K. Chakrabarti, R. A. Logan, J. Lopata, D. L. Van Haren, J. A. Long, and V. R. McCrary, *J. Cryst. Growth*, v109, p264, 1991.
- [11] D. Bertone, R. Y. Fang, G. Morello, and M. Meliga, *J. Electrochem. Society*, v146, no.3, p1167, 1999.
- [12] F. E. Ejeckam, C. L. Chua, Z. H. Zhu, Y. H. Lo, M. Hong, and R. Bhat, *Appl. Phys. Lett.*, v67, p3936, 1995.
- [13] A. R. Hawkins, W. Wu, P. Abraham, K. Streubel, and J. E. Bowers, *Appl. Phys. Lett.*, v70, p303, 1997.
- [14] J. J. Dudley, D. I. Babic, R. Mirin, L. Yang, B. I. Miller, R. J. Ram, T. Reynolds, E. L. Hu, and J. E. Bowers, *Appl. Phys. Lett.*, v64, p1463, 1994.
- [15] D. I. Babic, J. J. Dudley, K. Streubel, R. P. Mirin, J. E. Bowers, and E. L. Hu, *Appl. Phys. Lett.*, v66, p1030, 1995.
- [16] I.-H. Tan, J. J. Dudley, D. I. Babic, D. A. Coldren, B. D. Young, E. L. Hu, J. E. Bowers, B. I. Miller, U. Koren, and M. G. Young, *IEEE Photonics Technol. Lett.* v6, p811, 1994.
- [17] F. A. Kish, F. M. Steranka, D. C. DeFevere, D. A. Vanderwater, K. G. Park, C. P. Kuo, T. D. Osentowski, M. J. Peannasky, J. G. Yu, R. M. Fletcher, D. A. Steigwald, M. G. Craford, and V. M. Robbins, *Appl. Phys. Lett.*, v64, p2839, 1994.

- [18] G. E. Hofler, D. A. Vanderwater, D. C. DeFevere, F. A. Kish, M. D. Camras, F. M. Steranka, and I.-H. Tan, *Appl. Phys. Lett.*, v69, p803, 1996.
- [19] Y. H. Lo, R. Bhat, D. M. Hwang, M. A. Koza, and T. P. Lee, *Appl. Phys. Lett.*, v58, p1961, 1991.
- [20] E. Yablonovitch, D. M. Hwang, T. J. Gmitter, L. T. Florez, and J. P. Harbison *Appl. Phys. Lett.*, v58, p2419, 1990.
- [21] T. Chung, N. Hosoda, and T. Suga, *Appl. Phys. Lett.*, v72, p1565, 1997.
- [22] M. Shimbo, K. Furukawa, K. Fukuda, and K. Tanzawa, *J. Appl. Phys.*, v60, p2987, 1986.





## CHAPTER 4

### Optimization of the Active Layers

The characteristics of gain medium suitable for long wavelength vertical cavity surface emitting laser (LW-VCSEL) have been discussed at the beginning of this chapter. By considering material quality and limitations of process equipment, the InGaAlAs system lattice-matched to InP has been chosen as the active layers in this study. The optimized layer structures have been determined by investigating performance of edge emitting lasers (EELs) with InGaAlAs multiple quantum wells (MQW) as the active layers.

#### 4-1 Comparisons between Gain Materials in Long Wavelength Range

As shown in Figure 1-4, several kinds of material system can combine to emit light in long wavelength range. However, the most promising and conventional material systems lattice-match to InP substrate. As mentioned previously, the absence of high reflectivity distributed Bragg reflectors (DBRs) is the most challenge in making InP-based LW-VCSELs. Due to the well-developed AlAs/GaAs DBRs and the lower cost of GaAs substrates, numerous researchers have tried to develop GaAs-based gain materials in long wavelength range, which will be briefly discussed in this section. The fundamental properties of the InP-based gain materials will also be discussed.

##### GaAs-Based Gain Materials

It has recently been shown that the huge band-bowing present in the GaAsN system leads to a strong suppression of the GaAs bandgap with the addition of small amounts (~few percent) of N [1]. The expected dependence of bandgap on alloy

composition is illustrated in Figure 1-4. The additional N in InGaAs is expected to not only suppress the bandgap energy of InGaAs but also to compensate the compressive strain from In, enabling a greater concentration of In to be incorporated without relaxation, further increasing the wavelength. Besides allowing 1.3  $\mu\text{m}$  AlGaAs/GaAs-based DBRs to be integrated with 1.3  $\mu\text{m}$  active regions in a single epitaxial growth run, it would also provide advantages in electron confinement in the active region for better high-temperature performance (i.e., higher  $T_o$ ) [1], which would provide a distinct advantages over wafer-fusion processes.

Kondow et al. [1] proposed this system for application to 1.3  $\mu\text{m}$  laser diodes and VCSELs. They later demonstrated growth of GaNAs alloys with up to 10% nitrogen incorporation [2], with photoluminescence at around 1.3  $\mu\text{m}$ . Later this same group reported the first EEL, operating pulsed at room temperature [3], and then continuous-wave (CW) operations [4]. While the initial reports of InGaNAs lasers were made with GSMBE-grown material, more recently InGaNAs-based lone-wavelength laser diodes have also been demonstrated with MOCVD-grown material [5]. Progress in realizing 1.3  $\mu\text{m}$  VCSELs with this approach has been rapid. The Hitachi group reported CW photopumped lasing at 1.22  $\mu\text{m}$  and 1.25  $\mu\text{m}$  in a VCSEL structure containing an  $\text{In}_{0.3}\text{Ga}_{0.7}\text{N}_{0.007}\text{As}_{0.993}$  QW active region and AlGaAs/GaAs-based DBRs [6, 7]. Recently, this group reported pulsed electrically injected lasing from a similar doped structure [8]. As DBR designs are further refined, and active region optical efficiency is optimized, this approach becomes the new standard for 1.3  $\mu\text{m}$  VCSELs on GaAs substrates. The optical efficiency for longer wavelength, e.g. 1.5  $\mu\text{m}$ , is still low for InGaNAs materials, though; this approach requires more studies in the epitaxial growth conditions and understanding balance between high strain materials before it can get into longer wavelength.

## InP-Based Gain Materials

Monolithically grown DBRs lattice-matched to InP continued to attract interests due to the well existing highly efficient InGaAsP and InGaAlAs gain materials covered the wavelength window from 1.3 to 1.8  $\mu\text{m}$ . The InGaAsP material systems have been applied for buried heterostructure (BH) type long wavelength EELs for a long time. The quaternary feature makes this material easy to tailor different strain and emission wavelength. The InGaAlAs material system, which developed later [9], also shows good performance in laser operations. We have used a commercialized laser simulation software developed by Crosslight Software Inc. to calculate the gain behavior and laser characteristics in this study. The simulation software is introduced in appendix A-1. We first compare the gain-spectrum and gain-carrier concentration relation between InGaAlAs and InGaAsP material for a single quantum well structure with a thickness of 5 nm and a compressive strain of 1.5%. The emission wavelength is calculated to be 1.51  $\mu\text{m}$  when considering the quantum size effect and strain splitting effect as mentioned in chapter 2. The barrier is 10 nm thick and 0.75% tensely strained for compensating the strain in quantum well. No additional loss and confinement factor are assumed. The many body effect is neglected. The carrier recombination and emission above the barrier are also neglected. The temperature for calculation is 300 K. The injected carrier density ranges from  $1 \times 10^{16}$  to  $5 \times 10^{18} \text{ cm}^{-3}$ . The simulated gain spectrums for TE mode are shown on the left side of Figure 4-1 with the gain-carrier concentration relations shown on the right side. No big difference can be distinguished between these two materials from the intrinsic gain behavior at this point.

We then construct a Fabry-Perot (FP) laser structure containing these two material systems for MQWs. The number of quantum wells and the amount of strain

is the same for two material systems. The lower threshold current and higher slope efficiency for InGaAlAs system was obtained. The simulated band diagrams under forward bias and above the threshold conditions are shown in Figure 4-2. The band offset ratio between conduction band and valence band is 0.72 for InGaAlAs and 0.36 for InGaAsP. Due to the larger conduction band offset for InGaAlAs system, the electrons have fewer chance to jump out of the quantum wells to become leakage current. The high potential barrier is very important for high temperature laser operations since the extra energy gained by the electrons increases the possibility for electron to over-ride the barrier potential. In contrast, the relatively large valence band offset in InGaAsP system prevents the holes with large effective mass and low mobility uniformly distributing over the multiple quantum wells [10], leading to enhanced losses and carrier wasting. The electrons and holes gather in the first quantum well near the p-type cladding layer as shown on the right side of Figure 4-2(b). The increased carrier densities further worsen the laser performance due to the Auger recombination loss. The smaller conduction band offset and non-uniformity of carrier distribution for InGaAsP lasers lead to higher threshold current and lower slope efficiency in comparisons to InGaAlAs lasers.

## **4-2 Characterization and Optimization of the Active Layers**

Since the high temperature characteristic is essential in LW-VCSELs, we thereby choose the InGaAlAs system for gain mediums in this study. In this section, the structures of InGaAlAs multiple quantum wells will be optimized by investigating the performance of corresponding EELs.

### **Fabrication of Long Wavelength FP EELs**

The typical laser structure is shown in Figure 4-3(a). All the epitaxial layers were

grown by MOCVD on S doped n-type InP substrates with exact orientation to  $\langle 100 \rangle$  direction. The laser structure consists of following layers: an 1  $\mu\text{m}$  thick n-type InP layer, an 100 nm thick n-type InAlAs layer served as inner cladding, a pair of 100 nm un-doped  $\text{Al}_x\text{Ga}_{1-x}\text{In}_{0.48}\text{P}$  confinement layers with x graded from 0.49 to 0.25, active layers with six compressively strained InGaAlAs quantum wells separated by five tensile strained InGaAlAs barrier layers, a 50 nm thick p-type InAlAs layer also served as inner cladding, a 50 nm thick p-type InGaAsP barrier reducing layer with emission wavelength of 1.3  $\mu\text{m}$ , and a 200 nm thick p-type InGaAs contact layer. The equivalent band diagram is illustrated in Figure 4-3 (b). The interface between InP and InAlAs belongs to type II alignment. The as-grown wafer with laser structure is then processed to form a simple ridge structure. Figure 4-4 illustrates the schematic process flows for simple ridge FP lasers. The first step is ridge formation using dry or wet chemical etching. Then, the  $\text{SiN}_x$  was deposited to protect the top surface except for the contact layer above the ridge, followed by the metallization for top and bottom sides. The processed wafer was then cleaved into 300  $\mu\text{m}$  by 300  $\mu\text{m}$  chips with both facets coated. The reflectivity of front and rear coating is 30% and 85%, respectively. Finally, the chips were mounted to TO-56 packages for final testing.

The scanning electron microscope (SEM) is commonly used to examine the geometry of microelectronics. Figure 4-5 is the profile of the 1550 nm laser. In order to maintain single transverse mode, the ridge width is smaller than 3  $\mu\text{m}$ . An additional etching stop layer is incorporated in order to precisely control the etching depth during ridge formation as step (b) shown in Figure 4-4. Normally, the emission wavelength of the etching stop layer is shorter than the lasing wavelength to avoid the absorption causing the increase of the internal loss. The vertical position of the etching stop layer directly influences the threshold current by the amount of lateral

diffusion current under the etching stop layer [11]. The precision control of the ridge depth by introducing the etching stop layer in the laser structure assures highly uniformity of the laser characteristics over the entire wafer.

Figure 4-6 shows the high temperature performance of 1550 nm and 1310 nm lasers. The characteristic temperature can be calculated to be 80K, which is better than the performance of lasers with InGaAsP quantum wells ( about 50 ~ 70K).

### **The Effect of Strain**

The  $\text{In}_x\text{Ga}_{1-x}\text{As}$  layer can be directly used for quantum wells for laser operated in 1500 nm band. However, only one variable in composition of this alloy needs to adjust the quantum well thickness simultaneously to achieve our target lasing wavelength. For a 5 nm quantum well lasing in 1500 nm band, the percentage of In has to be 0.37 with a compressive strain of 0.67%. The thickness of quantum well has to be reduced to further obtained higher compressively strain or vice versa. Thin quantum wells place great challenges to epitaxial systems. The incorporation of Al in InGaAs system increases the freedom of combinations. The  $\text{In}_{1-x-y}\text{Ga}_x\text{Al}_y\text{As}$  system, with two variables in composition, allows us to have fixed thickness of quantum wells and emission wavelength but various values of strain.

Figure 4-7 demonstrates the performance of lasers with different amount of compressive strains in MQWs. All the barriers are tensely strained to compensate the strain in QWs. The threshold current density is calculated when the laser operates without facet coating. The threshold current density is decreased about 40% when increasing the strain in QWs from 0.6% to 1.4%. Figure 4-8 shows the X-ray diffraction patterns of different strain-compensated MQWs. The positions of the satellite peaks tell the strain amount in laser structures. The improvement of the laser characteristics with highly-strained MQWs should arise from the deformation of the

valence band. As briefly introduced in chapter 2, the biaxial strain will induce band shifting and deformations. Here, we use the laser simulation software to calculate the band structures for the different strains in single quantum well using a  $4 \times 4$  Hamiltonian in  $k_p$  theory. Figure 4-9(a) and (b) show the simulated valence band structures for 2.0% strain and 0.7% strain in quantum well, respectively. The square dots represent the heavy hole bands and the cross dots represent the light hole bands. The lines are parabolic fittings near  $k = 0$  for each band. The calculated first heavy hole band in Figure 4-9(a) deforms much seriously than that in Figure 4-9 (b). Since most of the carrier transitions are from first conduction band to first heavy hole band, the reduced density of states in Figure 4-9 (a) results in lower threshold current density and higher differential gain. In addition, the much more irregular valence band curves in highly strained MQWs helps to reduce the probability of Auger recombination loss. If we check a little more in Figure 4-7, the slight increase of the threshold current has been observed with the compressive strain more than 1.5% in MQWs. We attributes that the product of this strain and QW thickness approaches the critical thickness. The induced defect and imperfection increase the non-radiative recombination in QWs, thus, degrade the laser performance. This implies that the strain in MQWs can't be increased further even the compensating scheme is introduced. Therefore, the strain of 1.4% in MQWs becomes the best choice in our study.

### **The Effect of QW number**

We have also fabricated 1550 nm lasers with different QW numbers. In typical EELs, the larger number of quantum wells will increase the confinement factor in the transverse direction and enhance the laser performance in high temperature operations. The calculated confinement factors with four to eight quantum wells are shown in

Figure 4-10. The confinement factor has increased 50% when the number of QWs increases from four to eight.

Two types of quantum wells have been fabricated and examined. For structure I, the thickness of the QW and barrier are 5.5 nm and 9.3 nm, and the strain of the QW and barrier are 1.37% and  $-0.6\%$ , respectively. For structure II, the thickness of the QW and barrier are 6 nm and 7 nm, and the strain of the QW and barrier are 1.4% and  $-0.8\%$ , respectively. The corresponding threshold current density with both facets coated has been shown in Figure 4-10. For quantum well structure I, the threshold current density has decreased about 26% with number of quantum wells from four to eight. The enhanced trend toward larger number of quantum wells seems to poise at eight or nine quantum wells. The relatively low enhancement in comparisons to the confinement factor might arise from the non-uniformity of the carrier distributions in quantum wells with more pairs.

Quantum well structure II, which contains larger strain amount in quantum wells, exhibits better performance when the number of quantum wells is six. However, the threshold current density increases a little when the number of quantum wells goes to eight. We try to explain this in terms of the net amount of strain. The strain effect will accumulate as the layer thickness increases. Thus, it's better to evaluate the net strain with summations of the product of strain and thickness for all layers. The net amount for structure II quantum well is 50% larger than that for structure I quantum well. Defects and imperfections might be easily introduced when the number of structure II quantum wells increases. Therefore, more delicate strain scheme has to be taken care in MQWs with pairs more than six.

### **The Effect of P-type Doping Amount**

During the optimizations of the active layer structures, we have found that the



P-type dopant will also influence the laser performance. Figure 4-11 shows that the threshold current density has reduced 20% when the flow rate of p-type dopant precursor (dimethyl-zinc, DMZn) decreases from 1.9 to 0.24 sccm. The maximum hole concentration in the MOCVD grown InP layer is about  $1 \times 10^{18} \text{cm}^{-3}$ . The hole concentration is about  $1 \times 10^{18} \text{cm}^{-3}$  when the flow rate of p-type dopant precursor is above 1 sccm. Therefore, the extra p-type dopant, Zn, in the InP layers becomes the interstitial impurity, which migrates in the crystal lattice rapidly and forms the non-radiative recombination center. The free-carrier absorption and non-radiative recombination loss increase the threshold current density. Therefore, caution needs to be taken to avoid the extra p-type dopant grown in the epitaxial layers.



## References

- [1] M. Kondow, K. Uomi, A. Niwa, T. Kitatani, S. Watatahiki, and Y. Yazawa, *Jpn. J. Appl. Phys.*, v35, p1273, 1996.
- [2] M. Kondow, K. Uomi, T. Kitatani, S. Watatahiki, and Y. Yazawa, *Jpn. J. Cryst. Growth.*, v164, p175, 1996.
- [3] M. Kondow, S. Nakatsuka, T. Kitatani, Y. Yazawa, and K. Uomi, *Jpn. J. Appl. Phys.*, v35, p5711, 1996.
- [4] K. Nakanara, M. Kondow, T. Kitatani, Y. Yazawa, and K. Uomi, *Jpn. Electron. Lett.*, v32, p1585, 1996.
- [5] S. Sato, Y. Osawa, T. Saitoh, and I. Fujimura, *Electron. Lett.*, v33, p1386, 1997.
- [6] M. C. Larson, M. Kondow, T. Kitatani, Y. Yazawa, and M. Okai, *Electron. Lett.*, v33, p959, 1997.
- [7] M. C. Larson, M. Kondow, T. Kitatani, K. Tamura, and M. Okai, *IEEE Photonics Technol. Lett.*, v9, p1549, 1997.
- [8] M. C. Larson, M. Kondow, T. Kitatani, K. Nakahara, K. Tamura, H. Inoue, and M. Okai, *Postdeadline Abstracts from the 1997 Meeting of the Lasers and Electro-Optics Society (LEOS), San Francisco, CA*, Paper PD1.3, 1997.
- [9] C. E. Zah, R. Bhat, B. N. Pathak, F. Favire, W. Lin, M. C. Wang, N. C. Andreadakis, D. M. Hwang, M. A. Koza, T. P. Lee, Z. Wang, D. Barby, D. Flanders, and J. J. Hsieh, *IEEE J. Quantum Electron.*, v30, no.2, p511, 1994.
- [10] J. Piprek, P. Abraham, and J. E. Bowers, *Appl. Phys. Lett.*, v74, no.4, 1999.
- [11] J. Piprek, P. Abraham, and J. E. Bowers, *IEEE J. Quantum Electron.*, v36, no.3, p366, 2000.

## CHAPTER 5

### Fabrication of the Distributed Bragg Reflectors

Chapter 5 reports several different fabrication methods for DBRs used in long wavelength range. The optical and electrical properties of different DBRs will also be studied. Followed by the comparisons of novel InP/InGaAlAs and conventional InAlAs/InGaAlAs DBRs, the extremely high reflectivity mirror made by InP/Air-gap DBRs will be discussed.

#### 1-1 Comparisons of InP/InGaAlAs and InAlAs/InGaAlAs

##### Distributed Bragg Reflectors

###### Introduction

Long wavelength (1.3-1.5  $\mu\text{m}$ ) vertical cavity surface emitting lasers (VCSELs) are considered the best candidate for the future light sources in fiber communications. The advantages of VCSELs include single longitudinal mode output, small divergence circular emission beam profile, low power consumption and low cost reliable productions. The absence of high refractive index contrast in InP-lattice-matched materials impeded the progress of the development of 1.3-1.5  $\mu\text{m}$  VCSELs in comparison to the short wavelength (0.78-0.98  $\mu\text{m}$ ) VCSELs. Recently, long wavelength VCSELs have been successfully demonstrated with several different approaches. First, wafer fusion technique, that integrated the InP-based active layers and GaAs-based DBRs together, had been successfully realized for high performance long wavelength VCSELs [1, 2] but the capability of mass production is still questionable. Second, the InGaNAs 1.3  $\mu\text{m}$  VCSELs grown on GaAs substrates have been demonstrated with excellent characteristics [3, 4]. However, to extend the

InGaAs gain peak to beyond 1.5  $\mu\text{m}$  is rather difficult.

Monolithically grown DBRs lattice-matched to InP continued to attract interests due to the well existing highly efficient InGaAsP and InGaAlAs gain materials covered the wavelength window from 1.3 to 1.8  $\mu\text{m}$ . Metamorphic GaAs/AlAs DBRs lattice-matched to InP substrate have been applied to realize the long wavelength VCSELs [5, 6] but the inherent dislocations in metamorphic layers have impacts on the reliability of the devices. The Sb-based DBRs have large refractive index contrasts  $\Delta n$  ranging from 0.43 to 0.44 and have been successfully applied in the VCSEL structures [7, 8]. However, these DBRs have drawbacks such as the low thermal conductivity and relatively high growth complexity. The problem with the conventional InP-lattice-matched InP/InGaAsP and InAlAs/InGaAlAs is the small refractive index contrast ( $\Delta n = 0.27$  for InP/InGaAsP and  $\Delta n = 0.3$  for InAlAs/InGaAlAs) resulting in a larger number of DBR pairs required to obtain high reflectivity. In addition, using the conventional DBRs, not only the penetration depth will increase causing more absorption, but the heat dissipation is also a problem.

Recently, the DBRs based on relatively large refractive index contrast ( $\Delta n = 0.34$ ) material combination of InP/InGaAlAs have also been demonstrated [9-11]. This material combination not only has larger refractive index contrast than the conventional InP/InGaAsP and InAlAs/InGaAlAs material systems, but it also has other benefits including the smaller conduction band discontinuity, which is good for n-type DBRs, and the better thermal conductivity due the binary alloy of InP. However, the InP and InGaAlAs belong to different group V based materials. Problems like the As carry over, the transitional interface, and lateral uniformity will affect the quality of the epitaxial layers and the reflectivity of the DBRs. As a result, the challenge of growing this combination relies on perfect switching between InP

and InGaAlAs.

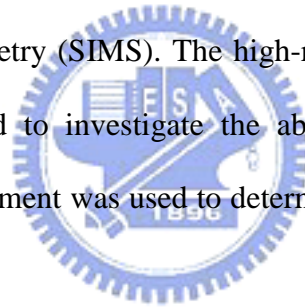
The growth interruptions have been frequently used in the metal organic chemical vapor deposition (MOCVD) growth of the InGaAs/InP or InGaAs/InGaAsP quantum wells in order to obtain abrupt interface [12, 13], but the growth of the InP/InGaAlAs DBRs using growth interruptions has not been investigated. In this paper, we report the effect of the growth interruptions on fabrication of the InP/InGaAlAs DBRs. The lateral uniformity and the reflectivity of the DBRs are very sensitive to the stabilization time of each terminated interface. We incorporated an in situ laser reflectometry while growing DBRs with thickness more than 8  $\mu\text{m}$  to insure minimum fluctuation in the center wavelength of the stopband. The optically pumped 1.56  $\mu\text{m}$  VCSELs with 35 pairs InP/InGaAlAs DBRs achieved stimulated emission at room temperature with the threshold pumping power of 30 mW.

### **Experimental Procedure**

All structures were grown in a vertical type low pressure MOCVD system with a rotating disk. The disk rotated at 900 revolutions per minute to maintain the laminar gas flow. The growth pressure was 70 torr. The growth temperature was 625 °C. V/III ratio was 150 for InP and 200 for InGaAlAs. The growth rate was 36.5 nm/min and 35 nm/min for InP and InGaAlAs, respectively. The alkyl sources were Trimethylindium, Trimethylgallium, and Trimethylaluminum, and the group V gases were AsH<sub>3</sub> and PH<sub>3</sub>. The carrier gas was hydrogen. Si<sub>2</sub>H<sub>6</sub> was used as the precursor of the n-type dopant. The epitaxial layers were all grown on n-type (100) InP substrates. The growth interruption between the InP and InGaAlAs had been divided into three steps. In the first step, the gases flowing just after the growth were hydrogen and the group V source used in the previous layer but with half of the flow rate for different period of  $t_p$  minute. Then, the group V source was switched off. The hydrogen was

kept flowing for 0.02 minute in the second step to remove the remaining group V source in the reactor. After that, the other group V source with the same flow rate used in the next layer was switched on with the hydrogen flowing for 0.01 minute in the third step to prepare the growth environment. Five different periods ( $t_p = 0, 0.1, 0.2, 0.3$  and  $0.4$  minute) of interruption were examined.

The optical microscope with the magnification of 120 examined the as-grown wafers first to check the lateral uniformity. The spectrometer was used to determine the reflectivity of the DBRs. The reflectivity of the Au film was used as the reference. The crystal quality and the lattice mismatch of the DBRs were analyzed by the double crystal X-ray. The thickness of each layer and the vertically compositional profiles were investigated by the field emission scanning electron microscope (SEM) and the secondary ion mass spectrometry (SIMS). The high-resolution transmission electron microscope (TEM) was used to investigate the abruptness of the interface. The current-voltage (I-V) measurement was used to determine the resistance of the n-type doped DBRs.



## Results and Discussion

The DBRs with ten pairs InP/InGaAlAs designed for  $1.55 \mu\text{m}$  VCSELs were first grown and investigated. The quarter-wavelength thickness of InP and InGaAlAs was  $122 \text{ nm}$  and  $110 \text{ nm}$ , respectively. To avoid the absorption of DBRs while the operating wavelength was  $1.55 \mu\text{m}$ , the lattice matched  $\text{In}_{0.53}\text{Ga}_{0.39}\text{Al}_{0.08}\text{As}$  was used with a band gap emission wavelength of  $1.42 \mu\text{m}$ . Figure 5-1(a) summarizes the surface conditions of 10 pairs InP/InGaAlAs DBRs grown with different interruption time  $t_p$  under the examinations by the optical microscope with the magnification of 120. When there was no interruption time ( $t_p = 0$  minute), pits with diameter ranging from  $0.5 \mu\text{m}$  to  $2 \mu\text{m}$  appeared densely on the surface of the as-grown wafer. When  $t_p$

increased to 0.4 minute, the pits decreased to fewer than 100 per square centimeter. A DBR structure grown with 0.1-minute interruption time was investigated by SEM and the picture of the cross section is shown in Figure 5-1(b). The arrow indicates the location where the pits occurred. Figure 5-2 shows the reflectivity curves of these samples measured by the spectrometer. The maximum reflectivity of DBRs increased when the interruption time  $t_p$  becomes larger. However, the center wavelength and the width of the stopband remained unchanged. Figure 5-3 shows the X-ray diffraction pattern of a set of samples grown with different interruption time. The value of lattice mismatch of all samples was within 200 ppm. Meanwhile, more intense satellite peaks are observed when the interruption time is longer. As far as the DBRs of the VCSELs are concerned, it is very critical to increase the reflectivity. The decrease of the reflectivity of the DBRs and the intensity of the satellite peak of the X-ray diffraction pattern with the shorter interruption time may be resulted from the scattering loss caused by the pits on the lateral interface. Nevertheless, the small differences in the width of the stopband in the reflectivity curves among five samples showed that the layer compositions in the vertical direction did not vary a lot indicating the abruptness between the interfaces was intact. The SIMS results of InP/InGaAlAs DBRs grown with  $t_p = 0.2$  minute shown in Figure 5-4 suggest that the phenomena of As carry-over did not appear. Consequently, the degradation of the reflectivity of InP/InGaAlAs DBRs mainly relates to the growth interruption time. After an InP or an InGaAlAs layer has grown, the surface needs time to stabilize under the atmosphere of previous group V gas. Then, the next layer with alternate group V source can continue to grow. This is the different case from growing the InAlAs/InGaAlAs or AlAs/GaAs material system. When the interruption time is shorter than 0.1 minute, the atom of the group V source cannot completely occupy the

surface. Meanwhile the other group V source switches on and enters the vacant site. This lattice mismatch causes the formation of defects. The defects elongate upward to form the pits while the growth continues.

Figure 5-5(a) and (b) show the interface conditions of the InP/InGaAlAs DBRs examined by TEM for two different growth interruption time. The growth sequence is indicated as the arrow direction. Figure 5-5(a) is for the optimized growth condition with interruption time of 0.3 minute. As can be seen the interfaces between the InP and InGaAlAs are clear and abrupt. Figure 5-5(b) shows the interfaces when the interruption time was 0 minute. Some dark clusters can be seen at the interface between the InGaAlAs and InP. However, the interface between InP and InGaAlAs did not contain these dark clusters. We attribute the dark clusters to the As carry-over effect when grown under the non-optimized growth condition. The lattice-mismatched InAsP formed at the interface and became defects. These defects elongated upward to form the pits while the growth continues and reduce the reflectivity of the DBRs. On the contrary, there is no need to consider the interface switching problems to grow the InAlAs/InGaAlAs DBRs. The abrupt interface can be obtained without the interruption time between consecutive layers. These results suggest that to grow the InP/InGaAlAs DBRs with high reflectivity, one need to add interruption time  $t_p$  more than 0.2 minute and make compromises between the total growth time, the amount of source usage and the required high reflectivity.

The DBRs with seven pairs n-type InP/InGaAlAs and InAlAs/InGaAlAs designed for 1.55  $\mu\text{m}$  VCSELs were then grown and investigated. The as-grown wafers were dry etched roughly 1.8  $\mu\text{m}$  down to the n-type InP substrate to form a round mesa with the diameter of 50  $\mu\text{m}$ . The periphery of the mesa was then passivated by  $\text{SiN}_x$ . After the thinning of the n-type InP substrate, the AuGe/Ni/Au



contacts were deposited on the both sides of the wafers. Figure 5-6(a) shows the I-V curves of the InP/InGaAlAs and InAlAs/InGaAlAs DBRs with round mesas of 50  $\mu\text{m}$  in diameter. The resistance per DBR pair is calculated to be  $1.2 \times 10^{-5} \text{ cm}^2$  and  $2.2 \times 10^{-5} \text{ cm}^2$  for InP/InGaAlAs and InAlAs/InGaAlAs DBRs, respectively. The lower value of the resistance of the InP/InGaAlAs is due to the smaller conduction band discontinuity (  $E_c = 0.15$  for InP/InGaAlAs and  $E_c = 0.47$  for InAlAs/InGaAlAs [14] ) between two layers. Figure 5-6(b) shows the simulated equilibrium band diagrams of the InP/InGaAlAs and InAlAs/InGaAlAs DBRs for the n-type concentration of  $1 \times 10^{18} \text{ cm}^{-3}$ . The results suggest that the voltage drop is mainly located at the interface to overcome the potential barrier. Further reduction in the resistance value can be achieved by modulation doping of the interfaces of the DBR structure to lower the potential barriers.

Next, two DBR structures with 35 pairs of InP/In<sub>0.53</sub>Ga<sub>0.39</sub>Al<sub>0.08</sub>As and 35 pairs of In<sub>0.52</sub>Al<sub>0.48</sub>As/In<sub>0.53</sub>Ga<sub>0.39</sub>Al<sub>0.08</sub>As were grown for comparisons. The interruption time  $t_p$  for growing InP/In<sub>0.53</sub>Ga<sub>0.39</sub>Al<sub>0.08</sub>As DBRs was chosen to be 0.4 minute. Fig. 5-7 shows the reflectivity curves of these two samples measured by the spectrometer. The measured reflectivity of samples was normalized to the reflectivity of the Au film. The maximum reflectivity of the InP/In<sub>0.53</sub>Ga<sub>0.39</sub>Al<sub>0.08</sub>As DBRs can reach over 99% and the width of the stopband is more than 100 nm, which is larger than the width of the In<sub>0.52</sub>Al<sub>0.48</sub>As/In<sub>0.53</sub>Ga<sub>0.39</sub>Al<sub>0.08</sub>As DBRs.

In summary, we have grown the InP/InGaAlAs and the InAlAs/InGaAlAs DBRs with excellent electrical and optical properties using MOCVD and the growth interruption technique. The DBRs show low resistance with an estimated resistance per DBR pair of  $1.2 \times 10^{-5} \text{ cm}^2$  and  $2.2 \times 10^{-5} \text{ cm}^2$  for InP/InGaAlAs and

InAlAs/InGaAlAs DBRs, respectively. The maximum reflectivity of both DBRs exceeds 99% with a stopband width of 110 nm for InP/InGaAlAs DBR and 100 nm InAlAs/InGaAlAs DBR. Although the InP/InGaAlAs DBRs have better optical and electrical properties, the InAlAs/InGaAlAs DBRs has much lower growth complexity. Both DBR structures should be applicable for fabrication of long wavelength VCSELs in 1.5~1.6  $\mu\text{m}$  range.

## **1-2 Distributed Bragg Reflectors for Long Wavelength VCSELs using InP/Air-gap**

Recently, using InP/airgap structure as DBR for 1.55  $\mu\text{m}$  VCSELs using InGaAs as sacrificial layer was reported [15, 16]. This structure has largest refractive index contrast of  $\Delta n = 2.16$  [17] and small optical loss in comparison to the conventional InP/InGaAsP and InAlAs/InGaAlAs material systems. The InP/airgap structure only requires 3 pairs to achieve high reflectivity of ~99.9%. However in the reported InP/airgap DBR structures, the wet etching solution of  $\text{FeCl}_3$  was used to etch the sacrificial InGaAs layer. The  $\text{FeCl}_3$  solution has relatively low selectivity between InGaAs and InP layers which could cause the decrease in the reflectivity and shifting the stop bandwidth center of the DBR. These reports also did not measure the actual reflectivity of InP/airgap DBRs. In this section, we report the fabrication and realization of a high reflectivity and rigid 1.55  $\mu\text{m}$  InP/airgap DBR using a new etching technique based on the superior etching selectivity and high etching rate of  $\text{H}_2\text{SO}_4$  solution for the InP/airgap DBR fabrication.

### **Design and Fabrication**

For a rigid InP/airgap DBR with high reflectivity, a thicker InP layer is preferable.

Our three-pair InP/airgap DBR structure has a  $\lambda/4$  thick InGaAs sacrificial layer and a  $5\lambda/4$  thick InP layer based on the simulation results. Figure 5-8 showed the calculated reflectivity of a three-pair InP/airgap DBR structure with three different InP layer thickness of  $\lambda/4$ ,  $3\lambda/4$ , and  $5\lambda/4$  for a fixed thickness of  $\lambda/4$  for the InGaAs layer. The result showed the peak reflectivity of three DBR structures has nearly the same high reflectivity value of 99.9 % around  $1.55\ \mu\text{m}$  while the stopband width gradually decreased with increasing InP layer thickness. For the  $5\lambda/4$  thick InP layer of DBR, the stopband still had a wide width of about 350 nm.

The 3-pair InP/InGaAs DBR structure with 615 nm ( $5\lambda/4$ ) thick of InP layer and 387 nm ( $\lambda/4$ ) thick of InGaAs layer was grown in a vertical type low pressure MOCVD system with a rotating disk. The disk rotated at 900 revolutions per minute to maintain the laminant gas flow. The growth pressure was 70 torr. The growth runs were carried out at a temperature of 625 °C. V/III ratio was 160 for InP and 75 for InGaAs. The growth rate was about 34 nm/min and 36 nm/min for InP and InGaAs, respectively. The alkyl sources were Trimethylindium (TMIn), Trimethylgallium (TMGa), and Trimethylaluminum (TMAI), and the group V gases were AsH<sub>3</sub> and PH<sub>3</sub>. Hydrogen was used as the carrier gas. The epitaxial layers were all grown on n-type (100) InP substrates. For growth of the InP and sacrificial InGaAs layers of DBR, the growth interruption time technique with an interruption time of 0.4 minutes based on our previous results [18] was used by switching gas flow between different group V sources. The double crystal X-ray measurement of the grown InP/InGaAs DBR structure showed clear satellite peaks indicating excellent crystal quality of the grown DBR structure.

The basic processing procedures of the fabrication of InP/airgap DBR are shown

in Figure 5-9(a) and (b). The MOCVD grown InP/InGaAs DBR structure was deposited with SiO<sub>2</sub> as dry etching mask by using plasma enhanced chemical vapor deposition (PECVD). Conventional photolithography was employed to define a 40 μm width of square mesas for supporting the InP/airgap structure with a 10 μm spacing openings. The openings were then dry etched by reactive ion beam etching (RIE). The etching conditions were set at 300 W total power under a 20 mTorr pressure with 10 sccm CH<sub>4</sub> /40 sccm H<sub>2</sub> /15 sccm Ar gas mixtures. The corresponding etching rates of InP and InGaAs were about 45 nm/min and 7 nm/min respectively. The time required for etching the whole DBR structure of about 4 μm depth was about 200 minutes. To prevent the accumulation of polymer during the RIE dry etching which has a deposition rate of about 3 nm/mins, a 10-minute clean-etching step is conducted using O<sub>2</sub> plasma between every 30 minutes of the CH<sub>4</sub> /H<sub>2</sub> /Ar RIE process. The procedure is important for maintaining the constant RIE dry etching rate [19, 20] for making the mesa with vertical sidewall. A vertical sidewall mesa is critical for uniform etching of the sacrificial InGaAs layers later and the formation of uniform airgap width to prevent any change in the reflectivity of InP/airgap DBR. After the mesa dry etching, the SiO<sub>2</sub> mask was removed by wet etching using HF solution.

The etching of InGaAs layers to form the air gap was conducted by wet chemical selective etching using a H<sub>2</sub>SO<sub>4</sub>: H<sub>2</sub>O<sub>2</sub>: H<sub>2</sub>O=1:1:2 solution. The solution has a good etching selectivity for InP and InGaAs and three times higher etching rate than the FeCl<sub>3</sub> solution. We used a spinning roller in the solution to increase wet etching uniformity and take away the reactant between the InGaAs layers. The airgap created by the wet etching process had a width of about 12.5 μm. The InP/airgap DBR structure was rinsed in D.I water and dried on the hot plate to clean up the residual water left in the air gap. Figure 5-10 depicts the SEM picture of the fabricated

InP/airgap DBR structure. The DBR structure has a rigid and stable structure with uniform air gaps.

### **Optical Characterization**

The reflectivity of the fabricated DBR structures was measured by the spectrometer. Figure 5-11 shows the reflectivity spectrum of the InP/airgap DBR structure. The dash line was the calculated curve and the solid line was the measured result. The peak reflectivity at the wavelength of 1540 nm with a stop-band width of about 200 nm was obtained. The measured stop-band width was narrower than the calculated width, which could be due to the limited etched airgap regions.

### **Thermal Analysis of LW-VCSELs with Air-gap Reflectors**

The large refractive index difference between InP and air is extremely suitable for making high reflection DBRs with few pairs. However, there is no heat dissipation path through the air gap within InP layers. The complex process steps usually require another kind of DBR (e.g. dielectric reflector) to implement a full VCSEL structure. As a result, the careful design of the VCSEL structures with air-gap reflectors becomes very important. In this subsection, we have applied finite element analysis to simulate the thermal modal for the VCSELs with air-gap reflectors and optimized the device structure when taking into account the thermal resistance and the optical loss.

The schematic cross section of LW-VCSEL with the air-gap and dielectric reflectors is shown in Figure 5-12. The thickness of the InP substrate is 100 nm. The radius of the InP substrate is 150  $\mu\text{m}$ . The air-gaps are formed by selectively etching off the InGaAs sacrifice layers. The etched off region termed undercut lay under the active region. The InP layer between the air-gaps is  $5/4\lambda$  thick, which can provide better mechanical support than the thickness of  $1/4\lambda$ . The half-wavelength thick active region made by InGaAlAs material system is sandwiched between InP spacer

layers. The multi-quantum-well (MQW) is the primary heat source at the threshold condition. The radius and the thickness of the MQW region are 5  $\mu\text{m}$  and 100 nm, respectively. The dielectric DBR with the radius of 8  $\mu\text{m}$  serves as the top mirror for the VCSEL.

With the known thermal conductivity and the laser operation conditions, the partial differential equation can be solved by finite element analysis software. The VCSEL is presumed to be junction-up packaged and maintains constant temperature (300K) at the bottom of the device. The other surfaces can be viewed as thermally isolated since the heat transfer efficiency through the air is rather low. The threshold current and voltage is assumed to be 5 mA and 1.2 V. The heat generation can be calculated to be  $7.64 \times 10^{14} \text{ W/m}^3$ . The simulated temperature distribution and the heat flow pattern are shown in Figure 5-13. The thermal resistance can be determined by the ratio of the maximum temperature rise in the MQW over the generated power of heat.

As shown in Figure 5-13, the air-gap reflectors block the heat flow. The radius of the undercut is critical for obtaining low thermal resistance. As shown in Figure 5-14(a), when the radius of the undercut gets smaller, the thermal resistance tends to be smaller. However, the radius of the undercut should not be smaller than the radius of the active region to avoid the scattering loss. Figure 5-14(b) and (c) show the influence of the p-InP and n-InP spacer layers on the thermal resistance. The increase of the thickness of the InP spacer layers is beneficial to lower the thermal resistance due to the relatively large thermal conductivity of the InP ( $k = 68 \text{ W/K.m}$ ). The thickness of the n-InP spacer layer is more detrimental to the thermal resistance since most of the heat flows downward to the substrate. From Figure 5-14(b) and 3(c), the thickness of the InP spacer layers has better to be greater than 1500 nm. In addition,

the metal contact on the top of the p-InP spacer layer can also provide good heat dissipation path due the large thermal conductivity of gold. The influence of the thickness of the metal contact is shown in Figure 5-14(d). The thermal resistance value of about 1100 K/W can be obtained when the radius of undercut is small and the thickness of the InP spacer layers and the metal contact is large. This value corresponds to 10K rise in the active region at the laser threshold condition.

The actual thermal resistance should be higher than the value calculated above due to the trench effect. In order to selectively wet-etch the InGaAs sacrifice layers, several trenches have to be formed around the active regions. These trenched can again block the heat dissipation path and increase the thermal resistance unless they are filled with InP by second overgrowth. Moreover, the increase of the thickness of the InP spacer layers will increase the optical loss. The calculated threshold gain versus the thickness of the InP spacer layers is shown in Figure 5-15. Since the absorption coefficient of the p-InP is six times larger than the n-InP, the optical loss increase dramatically with the thickness. To avoid the high optical loss in the p-InP spacer layer, the thickness of the p-InP spacer layer should be reduced. The alternative is to replace some parts of the p-InP spacer layer with n-InP spacer layer through the tunnel junction.

In summary, we have designed, fabricated, and demonstrated a rigid InP/airgap structure with high reflectivity at 1.54  $\mu\text{m}$  using InGaAs as the sacrificial layer. The 3-pair InP/airgap DBR structure with  $5 \lambda/4$  thick InP layer was fabricated from the MOCVD grown InP/InGaAs structure using  $\text{H}_2\text{SO}_4$  solution as etching agent. The InP/airgap DBR has a peak reflectivity at 1.54  $\mu\text{m}$  with a stop-band width of about 200 nm. The InP/airgap DBR structure was rigid and stable and should be applicable for 1.5  $\mu\text{m}$  VCSELs. In addition, the thermal modal of the LW-VCSEL with the

air-gap reflectors has been demonstrated. The radius of the undercut should be kept small to obtain better thermal resistance. Since the InP is a rather efficient thermal conductive material, increase the InP spacer layer could provide proper heat dissipation path. However, the high absorption coefficient of p-InP spacer layer could increase the optical loss. The thickness of the p-InP spacer should be reduced to avoid high optical loss. The alternative is to use the tunnel junction to replace the p-InP layer with n-InP layer. The thick metal contact could also provide good heat dissipation path.





## References

- [1] D. I. Babic, J. Piprek, K. Streubel, R. P. Mirin, N. M. Margalit, D. E. Mars, J. E. Bowers and E. L. Hu, *IEEE J. Quantum Electron.*, v33, no.8, p1369, 1997.
- [2] Y. Ohiso, C. Amano, Y. Itoh, H. Takenouchi and T. Kurokawa, *IEEE J. Quantum Electron.*, v34, no.10, p1904, 1998.
- [3] S. Sato, N. Nishiyama, T. Miyamoto, T. Takahashi, N. Jikutani, M. Arai, A Matsutani, F. Koyama and K. Iga, *Electron. Lett.*, v36, no.24, p2018, 2000.
- [4] G. Steinle, F. Mederer, M. Kicherer, R. Michalzik, G. Kristen, A. Y. Egorov, H. Riechert, H. D. Wolf and K.J. Ebeling, *Electron. Lett.*, v37, no.10, p632, 2001.
- [5] J. Boucart, C. Starck, F. Gaborit, A. Plais, N. Bouche, E. Derouin, J. C. Remy, J. Bonnet-Gamard, L. Goldstein, C. Fortin, D. Carpentier, P. Salet, F. Brillouet and J. Jacquet, *IEEE J. Sel. Topics Quantum Electron.*, v5, no.3, p520, 1999.
- [6] W. Yuen, G.S. Li, R.F. Nabiev, J. Boucart, P. Kner, R.J. Stone, D. Zhang, M. Beaudoin, T. Zheng, C. He, K. Yu, M. Jansen, D.P. Worland and C.J. Chang-Hasnain, *Electron. Lett.*, v36, no.13, p1121, 2000.
- [7] E. Hall, H. Kroemer and L.A. Coldren, *Electron. Lett.*, v35, no.5, p425, 1999.
- [8] E. Hall, S. Nakagawa, G. Almuneau, J.K. Kim and L.A. Coldren, *Electron. Lett.*, v36, no.17, p1465, 2000.
- [9] I. Sagnes, G. Le Roux, C. Meriadec, A. Mereuta, G. Saint-Girons and M. Bensoussan, *Electron. Lett.*, v37, no.37, p500, 2001.
- [10] M. Linnik and A. Christou, *IEEE Trans. Electron Devices*, v48, no.10, p2228, 2001.
- [11] M.H.M. Reddy, T. Asano, R. Koda, D.A. Buell and L.A. Coldren, *Electron. Lett.*, v38, no.20, p1181, 2002.
- [12] K. Streubel, J. Wallin, M. Amiotti, and G. Landgren, *J. Cryst. Growth.*, v124, p541, 1992.
- [13] K. Streubel, V. Harle, F. Scholz, and G. Landgren, *J. Appl. Phys.*, v71, p3300, 1992.
- [14] M.H.M. Reddy, T. Asano, R. Koda, D.A. Buell and L.A. Coldren, *Electron. Lett.*, v38, no.20, p1181, 2002;
- [15] E. Hall, S. Nakagawa, G. Almuneau, J. K. Kim, and L. A. Coldren, *Electron. Lett.*, v36, no.17, p1465, 2000.
- [16] N. Chitica, and M. Strassner, *Appl. Phys. Lett.*; v78, no.25, p3935, 2001.

- [17] Seng-Ticng Ho, S. L. McCall, R. E. Slusher, L. N. Pfeiffer, K. W. West, A. F. Levi, G. E. Blonder, and J. L. Jewell, *Appl. Phys. Lett.*, v57, no.14, p1387, 1990.
- [18] T.C. Lu, J.Y. Tsai, and S.C. Wang, *J. Cryst. Growth*, v250, p3-4, p305, 2003.
- [19] K. Streubel, S. Rapp, J. André, and N. Chitica, *J. Mater. Sci. and Eng. B*; v44, no.1-3, p364, 1997.
- [20] A. Boyde, and P. Vesely, *1972 Proceedings of the Annual Scanning Electron Microscopy Symposia, Chicago*, p266, 1972.



## CHAPTER 6

### Optically Pumped LW-VCSELs

The feasibility of the active layers and DBRs discussed in previous two chapters is examined by the performance of optically pumped LW-VCSELs. This chapter reports the structures and the characteristics of LW-VCSELs for optical pumping, including the InP-lattice-matched and wafer-fused structures.

#### 6-1 Structures and Characteristics of Optically Pumped LW-VCSELs

##### Based on InP/InGaAlAs DBRs

###### The Structure of LW-VCSEL

To further validate the viability of the DBR structures for long wavelength VCSELs, we have grown a laser structure based on the InP/InGaAlAs DBRs using the growth interruption technique. Figure 6-1 shows the laser structure. The epitaxial layers were grown on an n-type InP substrate. The first step was to grow the  $5/4\lambda$  thick InGaAlAs and InP calibration layers followed by the 35 pairs InGaAlAs/InP DBRs. The interruption time was 0.2 minute. The laser reflectometry monitored the epitaxial growth. The  $5/4\lambda$  thick InGaAlAs and InP calibration layers were first grown to check the growth rate and growth conditions before the entire DBRs were grown. The  $2\lambda$  thick periodic gain cavity was grown in the second step. At the same time, another InP dummy wafer was loaded in MOCVD for photoluminescence (PL) measurement. The laser structure has InGaAlAs cladding layers of  $2\lambda$  thick with a band edge emission peak at  $1.1 \mu\text{m}$ . Three sets of strain compensated multi-quantum wells (SCMQWs) were placed at the anti-nodes of the electric standing wave field within the  $2\lambda$  thick cavity to increase the enhancement factor of

MQW active regions. Each set of SCMQWs consisted of five InGaAlAs (strain = 1.37%, thickness = 5.5 nm) quantum wells and four InGaAlAs (strain = -0.6%, thickness = 9.3 nm) barriers and the PL wavelength was tuned at 1.51  $\mu$ m, which is 40 nm blue-shifted from the target emission wavelength to insure the proper operation of the VCSELs at room temperature [1]. Two InP space layers of half  $\lambda$  thickness grown on the top and the bottom of the cavity were served to protect the InGaAlAs layer from being oxidized during the post processing. Finally, the wafer was coated with 10 pairs SiO<sub>2</sub>/TiO<sub>2</sub> top dielectric mirrors to form a complete VCSEL structure.

### **The Results of Optical Pumping**

Figure 6-2 shows the reflectivity and PL measurements during every process step. All of the reflectivity results were normalized to the reflectivity of Au film. Figure 6-2(a) shows the reflectivity curve of 35 pairs InGaAlAs/InP DBRs. The center wavelength of the stop-band is located at 1555 nm. Figure 6-2(b) shows the reflectivity of the half cavity VCSEL. The PL spectrum of the active regions grown on the InP dummy wafer in the same run is shown in Figure 6-2(c). The PL peak is 1510 nm and the full width half maximum (FWHM) is 54 nm. The peak of shorter wavelength was the signal belonged to the previous grown layers on the InP dummy wafer. Figure 6-2(d) shows the reflectivity of the complete VCSEL structure and the Fabry-Perot dip is located at 1558 nm. Figure 6-2(e) demonstrates the PL spectrum of the complete VCSEL structure. The peak wavelength is coincided with the Fabry-Perot dip and the FWHM is measured to be 3.3 nm. The equivalent quality factor, Q, is estimated about 470 in the vertical direction.

The complete VCSEL structure was placed in an optical pumping system as shown in Figure 6-3. The pumping source was a continuous wave operated Ti:sapphire laser. The wavelength of the Ti:sapphire laser was tuned at 990 nm

although the pumping wavelength at slightly beyond 1.1  $\mu\text{m}$  would be more desirable to avoid absorption of the InP ( $\lambda_g = 0.9 \mu\text{m}$ ) space layers and InGaAlAs ( $\lambda_g = 1.1 \mu\text{m}$ ) cladding layers. The diameter of the pumping beam entered from the top dielectric DBRs was estimated to be 30  $\mu\text{m}$ . Figure 6-4 shows the pumping result of the VCSEL. The threshold pumping power is 30 mW at room temperature. The wavelength of the output beam is 1562 nm. The minimum linewidth above threshold is 1 nm limited by the resolution of the spectrometer. The red shift of the peak wavelength from the Fabry-Perot dip was attributed to the local heating caused by the strong absorption. The equivalent threshold current density is calculated to be 2  $\text{kA}/\text{cm}^2$  when taking into account the absorption of the pumping light in the cladding layers and the reflection at the surface. Compared this number with the best threshold current density obtained in chapter 4, which is about 1.45  $\text{kA}/\text{cm}^2$  shown in Figure 4-11, the relatively large threshold current density might be attributed to two reasons. One is the non-optimized quantum well structure in terms of the amount of net strain in periodic gain structure. The other is the relatively large cavity loss such as the absorption of the pumping power by the  $2\lambda$  thick cladding layers in the laser structure. All in all, the quality of the DBRs and the active region have been basically qualified in this demonstration for the first step in LW-VCSEL process.

## **6-2 Structures and Characteristics of Optically Pumped LW-VCSELs**

### **with Wafer-fused GaAs/AlAs DBRs**

High reflectivity DBR and high gain active region are important for LW-VCSEL. In this section, we first find the influence of the distance between fusion interface and active region on active region photoluminescence intensity. Second, we compare the

PL signal of the InGaAlAs MQW before and after fusion process. The reflectivity of DBR before and after fusion process is also compared. Finally, we demonstrate VCSEL structures with wafer-fused DBRs for optical pumping.

### **Influence of Distance between Fusion Interface and Active Region**

A stack of 290 nm InP / MQW / 290 nm InP / 180 nm InGaAs epitaxial layers as shown in Figure 6-5 was grown by MOCVD on InP substrate. The MQW structures consisting of a 70 nm  $\text{In}_{0.52}\text{Al}_{0.48}\text{As}$  inner cladding layer followed by six  $\text{In}_{0.39}\text{Ga}_{0.46}\text{Al}_{0.15}\text{As}$  barriers with thickness of 7 nm, and six  $\text{In}_{0.73}\text{Ga}_{0.2}\text{Al}_{0.07}\text{As}$  wells with thickness of 6nm, then another inner cladding layer  $\text{In}_{0.52}\text{Al}_{0.48}\text{As}$  with thickness of 70 nm. The two InP layers served as spacers. InGaAs was the etching stop layer. Another wafer was grown with 25 pairs of GaAs/AlAs on a GaAs substrate.

Before the fusion process, the samples were cleaved into four pieces with dimension of  $10*12 \text{ mm}^2$ . Three of these four samples were subsequently wet etched to change the thickness of the top InP layers. The top InP layers of these four samples are 290 nm, 190 nm, 140 nm and 90 nm. These four samples were fused with GaAs wafers with dimension of  $10*12 \text{ mm}^2$  at  $600^\circ\text{C}$  for one hour in hydrogen atmosphere. After fusion, the InP substrates and InGaAs stop layers were selective wet chemical etched with  $\text{HCl} : \text{H}_2\text{O} = 3 : 1$  and  $\text{H}_2\text{SO}_4 : \text{H}_2\text{O}_2 : \text{H}_2\text{O} = 1 : 1 : 10$ . The process flowchart was shown in Figure 6-5.

Dependence of the PL peak intensity on the distance from the fusion interface is shown as Figure 6-6. The PL peak intensity decreases as the distance from the interface decreases. It has been shown by Ram et al [2] that all dislocations occurring during fusion are localized to within 200 nm from the fused junction. The migrating dislocation might degrade the crystal quality and decrease the PL peak intensity. The dislocations that migrate to MQW increase as the distance from the interface decrease

along with the decrease of the PL peak intensity. Therefore, we should take the distance between fusion interface and active region into consideration when we design the VCSEL structure.

### **Comparisons of Spectra before and after Wafer Fusion Process**

The MQW wafer with the same structure in the last subsection was grown. Another wafer is the DBR consisting of a stack of 25 pairs 115 nm GaAs / 132 nm AlAs layers with grown on GaAs substrate by MOCVD. Before the fusion process, the MQW and DBR wafers were cleaved into 10\*12 mm<sup>2</sup> pieces. The PL of one MQW sample was measured using a 532 nm laser with 4.4 mW. The reflectivity of one DBR sample was also measured. After the fusion process with the MQW and DBR samples at 600°C in hydrogen atmosphere, the InP substrate and InGaAs etch stop layer were removed by wet etching. The process flowchart is shown in Figure 6-7.

Figure 6-8 shows the PL spectra of the sample before and after the wafer fusion. Due to the high reflectivity of the DBR, the PL peak intensity of the sample after fusion was 4.4 times higher than that before fusion process. The peak wavelength of MQW retained at 1521 nm after fusion process. The FWHM of the PL curve for the sample after fusion is 29 nm which is narrower than that (63 nm) of sample before fusion. An optical resonant cavity was formed after the fusion, which modified the peak wavelength and shrink the PL FWHM.

The DBR reflectivity spectra before and after fusion process are shown in Figure 6-9. The stop-band width of the DBR is the same before and after the fusion process. The maximum reflectivity of DBR is higher than 95%. As mentioned before, stop-band width and maximum reflectivity of DBR are very important for VCSEL device. It was confirmed that the fusion process does not affect these two key characteristics of DBR.

## Optical Pumping of VCSEL Structure with Double-fused DBRs

The fusion process flow chart of double-fused VCSEL structure is shown in Figure 6-10. The bottom mirror is a 30-period GaAs/AlAs DBR. The active region is a periodic gain structure consisting of three sets of five InGaAlAs quantum wells and barriers. The three sets of MQW are located at where the antinodes of standing wave pattern locate in the resonant cavity. The top mirror is a 25-period GaAs/AlAs DBR. One distinct feature is that the cavity length of the wafer-fused VCSEL structure has to be  $m\lambda + 0.5\lambda$  ( $m = 0, 1, 2, \dots$ ) to avoid the anti-node of the electrical field locating at the fusion interface to prevent strong absorption. In addition, the top layer of the DBRs has to be GaAs to avoid the oxidation of AlAs layers during the fusion process. The designed VCSEL structure is shown in Figure 6-11.

Before fusion process, the MQW and DBR wafers were cleaved into  $10 \times 12 \text{ mm}^2$  pieces. After pre-fusion process as mentioned in the previous section, the MQW and bottom DBR wafers were fused at  $600^\circ\text{C}$  in hydrogen at one atmosphere. After first fusion process, the InP substrate and InGaAs etch stop layer were removed by wet etching. In the second fusion process, the fused sample was fused with another 25-period GaAs/AlAs top DBR with a 30 nm InGaP stop layer. Then the GaAs substrate and the InGaP stop layer were removed by wet etching sequentially.

The final double-fused VCSEL was placed in the optical pumping system. The setup of optical pumping system is as the same as mentioned in the last section. The wavelength of the pumping laser was tuned at 900nm with 0.2 pico second pulses and a repetition rate of 76 MHz. Figure 6-12 shows the pumping result of the double-fused LW-VCSEL. The threshold pumping power density is about  $5 \text{ kW/cm}^2$  at room temperature. The inset shows the VCSEL emission spectrum at the pumping power density of  $8 \text{ kW/cm}^2$ . Peak emission wavelength is 1527 nm and the FWHM is 1.8 nm. The equivalent threshold current density is calculated to be  $4 \text{ kA/cm}^2$ . We



believe that this two-fold value compared with the previous threshold current density comes from the strong absorption of pumping light. The relatively thick top DBR absorbs some percentage of the incident light. The fusion interfaces, especially the top one, play an important recombination center for the pumping light due to the induced defects and QW-like band discontinuity at the fusion interfaces.



## References

- [1] J. Piprek, Y. A. Akulova, D. I. Babic, L. A. Coldren and J. E. Bowers, *Appl. Phys. Lett.*, v72, no.15, p1814, 1998.
- [2] R. J. Ram, J. J. Dudley, J. E. Bowers, L. Yang, K. Carey, S. J. Rosner, and K. Nauka, *J. Appl. Phys.*, v78, no.6, p4227, 1995.



## CHAPTER 7

### Electrically Driven LW-VCSELs

This chapter reports several different approaches to make electrically driven LW-VCSELs, including monolithically InP-based and wafer-fusion type devices. The ion-implantation or buried tunnel junction were used to make current apertures in these devices. The ion-implantation was applied to both InP-based and wafer-fusion type LW-VCSELs, while buried tunnel junction was integrated in a monolithically InP-based long wavelength light emission device. The structures and characteristics of these devices are discussed in this chapter.

#### 7-1 Fabrication of LW-VCSELs by Ion-implantations

After the verification of the LW-VCSEL structure by optical pumping discussed in the previous chapter, the next step is to fabricate electrically driven laser diodes. Ion-implantation has long been an easy and stable fabrication method in 850 nm VCSEL industry. In this section, we'd like to discuss the structure and experimental results of the InP-based LW-VCSEL with a Si-implantation current aperture.

##### The Structure of LW-VCSEL

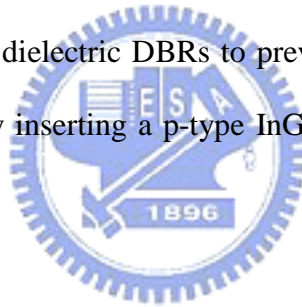
Figure 7-1(a) shows the laser structure. The epitaxial layers were grown on an n-type InP substrate. The first step was to grow 42 pairs InGaAlAs/InP DBRs. The interruption time was 0.2 minute. The quarter-wavelength thickness of InP and InGaAlAs was 122 nm and 110 nm, respectively. To avoid the absorption of DBRs while the operating wavelength was 1.55  $\mu\text{m}$ , the lattice matched  $\text{In}_{0.53}\text{Ga}_{0.39}\text{Al}_{0.08}\text{As}$  was used with a band gap emission wavelength of 1.42  $\mu\text{m}$ . The laser reflectometry in-situ monitored the epitaxial growth. Then, the  $3/4\lambda$  thick n- and p-type InP spacers

for phase matching were grown. The half-wavelength thick cavity was sandwiched between InP spacers. The cavity consisted of n- and p-type InAlAs inner cladding layers and strain compensated multiple quantum wells (SCMQWs). The SCMQWs consisted of seven InGaAlAs (strain = 1.4%, thickness = 6 nm) quantum wells and eight InGaAlAs (strain = -0.8%, thickness = 7 nm) barriers and the photoluminescence (PL) wavelength was 1551.5 nm with the FWHM of 108.3 nm. The wafer was then sent to ion-implantation with Si after aperture mask patterning. The diameter of the aperture was 28  $\mu\text{m}$ . The Si ions can compensate the p-type dopant and even make the InP layer to become n-type outside the aperture to form current blocking regions. The energy of the implanting ions is 100 KeV. The peak concentration of the Si in InP spacer layer located at about 100 nm away from the wafer surface measured by the secondary ion mass spectrometry (SIMS). Next, the wafer was passivated with  $\text{SiN}_x$  and coated with metal contacts for both sides. The emission aperture was 10  $\mu\text{m}$  in diameter. Finally, the wafer was coated with 10 pairs  $\text{SiO}_2/\text{TiO}_2$  top dielectric mirrors to form a complete VCSEL structure. The schematic of LW-VCSEL structure with a Si-implanted current aperture is shown in Figure 7-1(b).

## Results and Discussion

The voltage and emission light output versus driving current characteristics are shown in Figure 7-2. The solid lines in Figure 7-3 are the reflectivity and PL curves measured with only the half-cavity, which is the as-grown structure shown in Figure 7-1(a). The PL peak is 1547.4 nm with FWHM of 38.6 nm in comparisons to 108.3 nm for PL curve of the original MQW. The shrinkage of the FWHM demonstrated the increased quality factor of the cavity provided by the high reflectivity bottom DBR. However, this device did not show stimulated emission under the continuous-wave

(CW) operation. The emission output light saturated above 8 mA. The dashed line in Figure 7-3 is the electro luminance (EL) curve for the device. The FWHM of the EL spectrum is 36.9 nm with peak of 1518.0 nm for the full LW-VCSEL structure. The nearly unchanged FWHM and the quality factor of the full LW-VCSEL structure represented the ill function of the top mirror and large optical loss inhibiting the lasing operation. We have found that the top dielectric mirror degraded rapidly after the forward current applied. The degraded top dielectric mirror also changed the original phase matching condition in the half cavity structure, and thus the emission peak of EL spectrum for the full VCSEL structure has shifted. The relatively high operation voltage might arise from the poor p-type contact and caused more heat in the small aperture. To further modify this type of structure, we need to find more stable material conditions for dielectric DBRs to prevent the mirror degradation and improve the p-type contact by inserting a p-type InGaAs for contact layer to reduce the operation voltage.



## **7-2 Long Wavelength Light Emitting Diodes with Buried Tunnel**

### **Junctions**

#### **Introduction**

The buried tunnel junctions have been applied in many opto-electronic devices, such as multi-junction solar cells [1], multi-layer GaAs lasers [2-5], vertical cavity surface emitting lasers [6] and GaN based blue light emitting diodes [7]. Introducing buried tunnel junctions in LW-VCSELs has two main advantages. First, the buried tunnel junction allows selective tunneling current injection and the areas without the tunnel junction automatically serve as the current blocking function. In comparisons to the ion-implantation, the buried tunnel junction provides precise aperture location

inside the LW-VCSEL structure. Second, the buried tunnel junction exhibits higher effective refractive index for the current aperture providing index-guiding effect as discussed in chapter 2. In this subsection, we'd like to discuss the initial attempt to fabricate the lone wavelength light emitting diodes (LEDs) with buried tunnel junctions before we fabricated the LW-VCSELs with tunnel junctions.

### **The Structure of Long Wavelength LEDs with Buried Tunnel Junctions**

Figure 7-4(a) shows the epitaxial structure. The epitaxial layers were grown on an n-type InP substrate. The half-wavelength thick cavity with the same structure as discussed in the previous subsection was sandwiched between InP spacers. The cavity consists of n- and p-type InAlAs inner cladding layers and SCMQWs. The PL wavelength was 1531.9 nm. After that, the half-wavelength thick p-type InP layer was grown followed by the  $p^{++}/n^{++}$  tunnel junction. The top layer was a thin n-type InP layer for protection. The tunnel junction layers consisted of an InGaAlAs (20 nm,  $\lambda_g = 1425$  nm) heavily doped  $p^{++}$  layer and 2 period InGaAs/InP (4 nm/4 nm) modulation doped  $n^{++}$  layers as shown in Figure 7-4(b). The tunnel junction is necessary to be in the nodes of the standing electromagnetic wave inside the VCSEL cavity to prevent large internal loss. The buried tunnel junction located on the top of the aperture serves as the window area assisting current flowing from p-type InP space layer to n-type InP contact layer. That is, both contacts of the device are n-type, except that the top contact is positively charged and the bottom contact is negatively charged. The schematic operation principal for the tunnel junction shown in Figure 7-4(c) explains the electron flow under the reverse bias condition. The wafer was then sent back to MOCVD for regrowth after desired aperture mesa was etched. The regrowth technique is discussed in chapter 3. The cross-section SEM image of the buried tunnel junction after the regrowth process with the smooth regrown surface is

shown in Figure 7-5(b). The diameter of the aperture was 30  $\mu\text{m}$ . Next, the wafer was passivated with  $\text{SiN}_x$  and coated with metal contacts for both sides. The metal contact aperture was 50  $\mu\text{m}$  in diameter. The schematic of lone wavelength light emitting diode structure with buried tunnel junction is shown in Figure 7-5(a). The top view of the devices is shown in Figure 7-5(c).

## Results and Discussion

Figure 7-6 successfully demonstrates the light emission power and voltage versus current characteristics for the lone wavelength light emitting diode with buried tunnel junction. However, this structure can be applied in LW-VCSELs before the operation voltage is lowered. The high operation voltage might arise from the low tunneling efficiency of the tunnel junction. Since the p-type dopant, Zn, is highly diffusive, the diffusion of Zn into heavily n-type doped area will compensate that area to form a graded junction. However, the abrupt junction interface is essential for tunneling current with low reverse bias voltage. Therefore, other p-type dopant with low diffusion characteristics, such as C, is more appropriate for heavily doping layer in tunnel junction. The C doping is relatively difficult in In-contained materials with percentage of In more than 50% [8]. The special epitaxial technique has to be established in the future.

### 7-3 Fabrication of LW-VCSELs by Wafer Fusion Techniques

#### Quantum Well Inter-mixing

Although the fabrication process of the electrically driven LW-VCSELs by wafer fusion was as the same steps described in chapter 6, large extent of PL blue-shift was observed after the fusion process. Since the fusion process take place in a high temperature environment, we have examined the temperature effect on the properties of the MQWs with doped and undoped spacer layers. Two samples were put into

MOCVD reactor for high temperature annealing with hydrogen and  $\text{PH}_3$  flowing for surface protection. Figure 7-7(a) shows the PL peak wavelength for the MQWs versus the post annealing temperature characteristics. Relatively large blue-shift was observed in MQWs with doped spacer layers. Figure 7-7(b) shows the X-ray diffraction patterns for the as-grown MQWs with doped spacer layers and the MQWs after 750 °C post annealing. The PL peak has blue-shifted for about 55 nm after 750 °C post annealing, though, the X-ray diffraction patterns did not alter very much, implying that the crystal periodicity still remained. This phenomenon has been studied as the quantum well inter-mixing or quantum well disordering effect [8-10]. Schematics of quantum well inter-mixing are shown in Figure 7-7(c). The Ga and Al atoms in quantum wells and barriers will inter-diffuse to each other to obtain thermal equilibrium at high temperature. This inter-diffusion has changed the shape and the energy band of the quantum wells thus lifted the energy band. However, the relative superlattice periods do not change. The quantum well inter-mixing effect is more strongly when there exists impurity such as p- or n-type dopant. This is also called impurity induced disordering. Therefore, this great amount of PL blue-shift has to be taken into account when considering the gain peak offset to the cavity mode in doped LW-VCSEL structure made by wafer fusion technique.

### **The Structure of LW-VCSELs by Wafer Fusion Techniques**

The epitaxial layers for cavity were grown on an n-type InP substrate. The  $1/2\lambda$  thick active region was sandwiched between  $1/2\lambda$  thick n- and p-type InP spacer layers. The active region consists of n- and p-type InAlAs inner cladding layers and SCMQWs. The SCMQWs consisted of seven InGaAlAs (strain = 1.4%, thickness = 5 nm) quantum wells and eight InGaAlAs (strain = -0.8%, thickness = 7 nm) barriers. The PL wavelength was 1294.8 nm with a FWHM of 56.5 nm. Two GaAs/AlGaAs



DBRs were grown by MOCVD separately. The n-type DBR consisting 30 pairs of GaAs/AlAs was fused with active region first. After removing the InP substrate, the sample was fused with p-type DBR consisting 25 pairs of GaAs/Al<sub>0.1</sub>Ga<sub>0.9</sub>As. The cross-section SEM image of the laser cavity with smooth fusion interfaces is shown in Figure 7-8(b). The wafer was then sent to ion-implantation with proton after aperture mask patterning. The diameter of the aperture was 30 μm. Next, the wafer was passivated with SiN<sub>x</sub> and coated with metal contacts for both sides. The metal contact aperture was 50 μm in diameter. The schematic of the double-fused LW-VCSEL with a proton-implanted current aperture is shown in Figure 7-8(a).

### Results and Discussion

Figure 7-9(a) shows the top emission image of the LW-VCSEL with double-fused DBRs. Figure 7-9(b) shows the EL spectrum measured from the top surface of the LW-VCSEL with a proton-implanted current aperture. The peak wavelength is 1288.8 nm with a FWHM of 5.6 nm, corresponding to a quality factor of 230. Unfortunately, the current-light output curve did not show features of stimulated emission. We have observed the relatively high series resistance and operation voltage. It's important to lower the series resistance before we can successfully fabricate this type of LW-VCSEL demonstrating continuous wave lasing. Optimization of the p-type doping in GaAs/AlGaAs DBRs and fusion conditions will be the initial steps in the future.

## References

- [1] G. C. DeSalvo, *J. Appl. Phys.*, v74, p4207, 1993.
- [2] J. P. van der Ziel and W. T. Tsang, *Appl. Phys. Lett.*, v41, p499, 1982.
- [3] A. R. Sugg, E. I. Chen, T. A. Richard, S. A. Maranowki and N. Holonyak, Jr., *Appl. Phys. Lett.*, v62, p2510, 1993.
- [4] J. J. Wierer, P. W. Evans, and N. Holonyak, Jr., *Appl. Phys. Lett.*, v71, p2286, 1997.
- [5] J. C. Garcia, E. Rosencher, P. Collot, N. Laurent, J. L. Guyaux, J. Nagle and E. Chirlias, *J. Crystal Growth*, v201/202, p891, 1999.
- [6] J. J. Wierer, P. W. Evans, N. Holonyak, Jr. and D. A. Kellogg, *Appl. Phys. Lett.*, v71, p3468, 1997.
- [7] T. Takeuchi, G. Hasnain, S. Corzine, M. Hueschen, R. P. Schneider, Jr., C. Kocot, M. Blomqvist, Y.-I Chang, D. Lefforge, M. R. Krames, L. W. Cook and S. A. Stockman, *Jpn. J. Appl. Phys.*, v40, pL861, 2001.
- [8] N. Watanabe, S. Yamahata, and T. Kobayashi, *J. Cryst. Growth*, v200, p599, 1999.
- [9] V. Hofsass, J. Kuhn, H. Schweizer, H. Hillmer, R. Losch, and W. Schlapp, *J. Appl. Phys.*, v78, no.5, p3534, 1995.
- [10] P. Offermans, P. M. Koenraad, J. H. Wolter, J. D. Song, J. M. Kim, S. J. Bae, and Y. T. Lee, *Appl. Phys. Lett.*, v82, no.8, p1191, 2003.

## CHAPTER 8

### Conclusions and Future Works

#### Conclusions

In this study, we have explored and developed the process for fabrication of long wavelength vertical cavity surface emitting lasers (LW-VCSELs). We have achieved the following benchmarks with the assistance of modern epitaxial technology provided by metal organic chemical vapor deposition (MOCVD) system.

##### **(1) Optimization of gain mediums:**

We have obtained impact factors for InGaAlAs based multiple quantum wells (MQWs). The amount of compressive strain strongly influences the threshold current density. However, the net strain amount has to be calculated and balanced when applying more quantum well numbers to increase the gain. In addition, the impurity concentration strongly influences the performance of edge emitting lasers (EELs) due to the extent of the internal loss. The overall optimization of these factors makes us obtaining low threshold current density of  $1.45 \text{ kA/cm}^2$  in EELs with  $300 \text{ }\mu\text{m}$  cavity length and 30%/85% facet coatings.

##### **(2) High reflectivity InP/InGaAlAs-based distributed Bragg reflectors (DBRs):**

We have grown InP/InGaAlAs and InAlAs/InGaAlAs DBRs with excellent electrical and optical properties using MOCVD and the growth interruption technique. The DBRs show low resistance with an estimated resistance per DBR pair of  $1.2 \times 10^{-5} \text{ }\Omega\text{-cm}^2$  and  $2.2 \times 10^{-5} \text{ }\Omega\text{-cm}^2$  for the InP/InGaAlAs and InAlAs/InGaAlAs DBRs, respectively. The maximum reflectivity of both DBRs exceeds 99% with a stopband width of 110 nm for InP/InGaAlAs DBR and 100 nm InAlAs/InGaAlAs DBR.

Although the InP/InGaAlAs DBRs have better optical and electrical properties, the InAlAs/InGaAlAs DBRs has much lower growth complexity. Both DBR structures should be applicable for fabrication of long wavelength VCSELs in 1.5~1.6  $\mu\text{m}$  range.

### **(3) High reflectivity InP/Airgap DBRs:**

We have designed, fabricated, and demonstrated a rigid InP/airgap structure with high reflectivity at 1.54  $\mu\text{m}$  using InGaAs as the sacrificial layer. The 3-pair InP/airgap DBR structure with 5  $\lambda/4$  thick InP layer was fabricated from the MOCVD grown InP/InGaAs structure using  $\text{H}_2\text{SO}_4$  solution as etching agent. The InP/airgap DBR has a peak reflectivity at 1.54  $\mu\text{m}$  with a stopband width of about 200 nm. The InP/airgap DBR structure was rigid and stable and should be applicable for 1.5  $\mu\text{m}$  VCSELs.

### **(4) Demonstration of fusion techniques:**

We have setup a wafer fusion system and established the wafer fusion techniques and process conditions. Smooth fusion interfaces have been observed with cross-section SEM images. The crystal quality of InGaAlAs MQW do not degrade. The reflectance spectra, stopband and maximum reflectivity of GaAs/AlAs DBR before and after fusion process do not change. Reliable fusion mechanical intensity, smooth fusion interface, and good optical and electrical characteristics of fusion interfaces provide good basement for further fabrication of LW-VCSELs.

### **(5) Successful demonstration of optically pumped InP-based LW-VCSELs:**

We also demonstrated the optically pumped InP-based VCSELs with the 35 pairs InP/InGaAlAs DBRs and 10 pairs  $\text{SiO}_2/\text{TiO}_2$  top dielectric mirrors and a  $2\lambda$  thick cavity composed periodic strain compensated MQWs to fully utilize the gain in every quantum well. The optically pumped VCSELs operated at room temperature with the

threshold pumping power of 30 mW. The wavelength of the output beam is 1562 nm. The minimum linewidth above threshold is 1 nm limited by the resolution of the spectrometer. The equivalent threshold current density is calculated to be 2 kA/cm<sup>2</sup> when taking into account the absorption of the pumping light in the cladding layers and the reflection at the surface.

**(6) Successful demonstration of optically pumped LW-VCSELs made by wafer fusion:**

We demonstrated the optically pumped VCSEL structure with the fused bottom 30 pairs GaAs/AlAs DBR, InGaAlAs MQW and the fused top 25 pairs GaAs/AlAs DBR. The optically pumped double fused VCSELs operated at room temperature with the threshold pumping power density of 5 kW/cm<sup>2</sup> and emitted laser at 1527nm. The equivalent threshold current density is calculated to be 4 kA/cm<sup>2</sup>. We attributed this two-fold value compared with the threshold current density obtained in InP-based LW-VCSEL to the strong absorption of pumping light.

**(7) Demonstration of regrowth and buried tunnel junction devices:**

We have demonstrated the prototype long wavelength light emitter with buried tunnel junction by regrowth technique in MOCVD reactor. Smooth regrown interface and flat wafer surface have been obtained. The preliminary emission shows the good current blocking scheme outside the buried tunnel junction area. The built-in index-guiding characteristics provided by the buried tunnel junction should be applicable in single mode LW-VCSELs.

**Future Works**

Although many benchmarks have been done, our long-term goal to fabricate electrically driven continuous wave (CW) LW-VCSELs with single mode operation has yet to be fulfilled. All previous steps will provide precious information and

experience in the future. To achieve this goal, the following actions require to be done:

**(1) Improvement of dielectric mirror quality:**

In hydride type of VCSEL, the quality of the dielectric mirror is important. When the device is electrically driven, the access heat and high surface carrier density between the epitaxial layer and dielectric mirror easily damage the surface and coating materials. The combinations of a-Si/Al<sub>2</sub>O<sub>3</sub> will be tested since they have larger refractive index difference and better thermal conductance in comparisons to the combinations of SiO<sub>2</sub>/TiO<sub>2</sub>.

**(2) Optimization of p-type contacts:**

The common feature in our electrically driven LW-VCSELs discussed in chapter 7 is the relatively high operation voltage. One main contribution of the high operation voltage is the poor ohmic condition of p-type contacts. The insertion of a small bandgap material, e.g. InGaAs, between the p-type metal contact and InP layer should be helpful to reduce the operation voltage.

**(3) Development of C doping in In-contained layers grown by MOCVD:**

To further increase the tunneling efficiency of the tunnel junction, the abrupt junction interface is essential for tunneling current with low reverse bias voltage. P-type dopant with low diffusion characteristics, such as C, is more appropriate for heavily doping layer in tunnel junction instead of the highly diffusive p-type dopant, Zn. Although the C doping is relatively difficult in In-contained materials with percentage of In more than 50% , the special epitaxial technique has to be established first in the future.

**(4) Optimization of serial resistance in p-type DBRs:**

In our demonstration of electrically driven double-fused LW-VCSEL, the

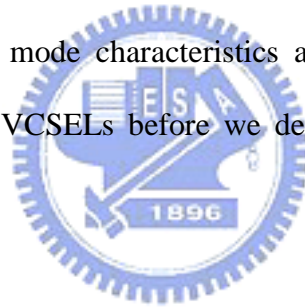
relatively high operation voltage is the main problem. Optimization of the p-type doping in GaAs/AlGaAs DBRs and fusion conditions will be the initial steps in the future.

**(5) Design and fabrication of air-gap type LW-VCSELs for optical pumping:**

LW-VCSELs with extremely high reflectivity air-gap DBRs is potentially applicable in wavelength tunable devices. However, the heat dissipation and current aperture formation are quite difficult. The regrowth technique and buried tunnel junctions can be further applied in the process of air-gap type VCSELs.

**(6) Analysis of transverse mode characteristics in LW-VCSELs:**

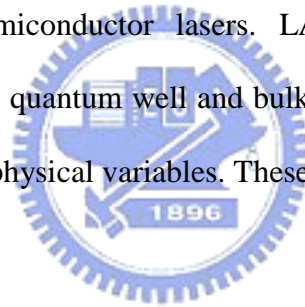
Single mode operation of VCSEL is very important in fiber communications. We need to study the transverse mode characteristics and understand more about the scheme of mode patterns in VCSELs before we design and fabricate single-mode LW-VCSELs.



# APPENDIXES

## A-1 Introduction to Laser Simulation Software

Crosslight Software includes a number of computer aided design simulation packages. These packages are designed to simulate semiconductor electronic or optoelectronic devices. LASTIP (LASer Technology Integrated Program), which is mostly used in this study, is a device simulation program designed to simulate the operation of a semiconductor laser in two dimensions (2D). Given the structural and material properties, it produces simulation data to describe the lasing characteristics. LASTIP can be used to model the electrical and optical behaviors on a 2D cross section of all types of semiconductor lasers. LASTIP solves the appropriate differential equations for both quantum well and bulk semiconductor lasers. LASTIP can be used to analyze many physical variables. These include four main categories in the following:



Carrier transport:

- Drift-diffusion model for electrons and holes including Fermi statistics
- Shockley-Read-Hall and Auger recombination
- Incomplete ionization of defects
- Deep level traps, dynamic models
- Carrier mobility as function of field, doping, and temperature
- Ohmic and Schottky contacts
- Hetero-junctions, thermionic emission
- Stimulated and spontaneous emission of photons
- Quantum tunneling models
- Energy balance model (hot carrier)



### Heat transfer:

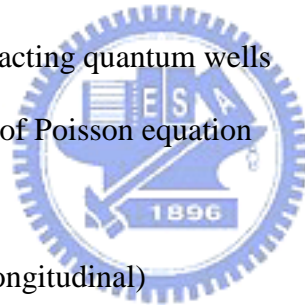
- Two dimensional temperature distribution, update of material parameters
- Joule heat, Peltier effect, Thomson effect
- Heating due to optical absorption and carrier recombination
- Including external thermal resistance

### Quantum well and bulk active regions

- 4×4 kp theory for valence band structure
- Strained quantum wells, valence band mixing
- Optical gain spectrum versus carrier density and temperature
- Gain broadening (Lorentz, Landsberg and Asada types)
- Carrier-carrier and carrier-phonon scattering mechanisms
- Non-symmetric and interacting quantum wells
- Self-consistent inclusion of Poisson equation

### Optical modes:

- Wave equation (lateral, longitudinal)
- Multimode operation
- Spatial hole burning
- Non-linear gain suppression model
- Far-field emission pattern
- Photon rate equation



## References

- [1] LASTIP user's manual, Crosslight Software Inc. v2003.12, 3<sup>rd</sup> ed.
- [2] Tutorial Workbook for LASTIP, APSYS, and PICS3D, 2003.04.
- [3] J. Piprek, *Semiconductor Optoelectronic Devices: Introduction to Physics and Simulation*, Academic Press, 2003.

